Surface & Coatings Technology 460 (2023) 129395

Contents lists available at ScienceDirect

Surface & Coatings Technology

journal homepage: www.elsevier.com/locate/surfcoat

Full Length Article

A new approach to improve some properties of wire arc additively manufactured stainless steel components: Simultaneous homogenization and boriding

Ali Günen [a,*], Uğur Gürol [b,c], Mustafa Koçak [d], Gürel Çam [e]

[a] Iskenderun Technical University, Faculty of Engineering and Natural Sciences, Department of Metallurgy and Materials Engineering, 31200 Iskenderun, Hatay, Turkey
[b] Istanbul Gedik University, Faculty of Engineering, Department of Metallurgical & Materials Engineering, Istanbul, Turkey
[c] Gedik Welding Company, Research and Development Center, Istanbul, Turkey
[d] Istanbul Gedik University, Faculty of Engineering, Dept. of Mechanical Engineering, Istanbul, Turkey
[e] Iskenderun Technical University, Faculty of Engineering and Natural Sciences, Department of Mechanical Engineering, 31200 Iskenderun, Hatay, Turkey

ARTICLE INFO

Keywords:
Wire arc additive manufacturing
Stainless steel
Gas metal arc welding
Boriding
High-temperature wear

ABSTRACT

Arc-directed energy deposition (Arc-DED), also commonly referred to as wire arc additive manufacturing (WAAM), is a cost-effective 3D metal additive manufacturing process in which large metallic parts can be produced due to high deposition rates. Stainless steels, widely used in many areas due to their excellent corrosion resistance, are one of the most produced materials by the WAAM method. However, stainless steels have low surface hardness. Moreover, the high heat input in the deposition process in WAAM sometimes causes the mechanical properties of stainless steels to be lower than casting or wrought stainless steels. These considerations limit the use of WAAM stainless steels, especially in abrasive environments. For this purpose, 307ER stainless steel produced by WAAM method was subjected to homogenization and boriding process simultaneously at 1000 °C for 1 h and the effect of applied heat treatment on microstructure, phase components, hardness and wear resistance was investigated. The results showed that with the boriding process, a 30 μm thick boride layer consisting of FeB, Fe_2B, Cr_5B_3 and MnB phases with a hardness of 21.5 GPa and a modulus of elasticity of 310 GPa was formed in addition to the dissolution of interdendritic regions in the as-built structure and a complete homogenization of the microstructure. Furthermore, owing to the high hardness and elasticity modulus in addition to the boride layer's self-lubrication properties obtained on the WAAM samples surfaces, 31.84 times and 8.06 times increased in wear resistance at room temperature and 500 °C temperature, respectively, and a decrease in friction coefficients was obtained. Moreover, the results showed that the simultaneous homogenization and boriding processes of stainless steels produced by the WAAM method would improve their microstructure and tribological behavior. This way, these steels can be used in wider areas of application.

1. Introduction

Additive manufacturing (AM) is an innovative manufacturing method based on the fabrication of a structurally complex three-dimensional (3D) component by gradually adding thin layers of material guided by a digital model [1,2]. The AM method allows the fabrication of complex components with higher efficiency (less material consumption) without using the molds required in traditional manufacturing methods such as casting and forging, as well as significantly increasing the flexibility of manufacturing of the products, especially those with complex geometries [3,4].

A laser beam, electron beam, or electric arc supplies the heat energy required to manufacture AM parts [5]. These heat sources used in the AM method have advantages and disadvantages compared to each other. In additive manufacturing practices where electron and laser beams, particularly laser beam, are used, energy control and the shape of the component to be formed have high precision. However, the deposition rate is low, and thus the production efficiency is limited in powder-bed metal-additive manufacturing processes, where laser and electron beam are used as heat sources [6]. In addition, metal powders used in powder-based laser or electron beam direct energy deposition methods are costly [5].

* Corresponding author.
E-mail address: ali.gunen@iste.edu.tr (A. Günen).

https://doi.org/10.1016/j.surfcoat.2023.129395
Received 9 January 2023; Received in revised form 23 February 2023; Accepted 27 February 2023
Available online 9 March 2023

On the other hand, wire arc additive manufacturing (WAAM) is a promising droplet-based additive manufacturing method [5], with high deposition rate for the direct production of large-scale complex parts [10]. In the WAAM method, a metal wire is melted continuously by a heat source to form a metal droplet, which is transferred into the melt pool to form a deposition layer [11]. The manufacturing process is completed when it is finally left to solidify at the molten pool boundary [2,9]. The wire material used in the WAAM process is 1/10 co of the cost of metal powders of the same weight. [5,7,8]. This allows AM parts to be produced at lower costs and in large-scale complex parts [10]. In addition, because WAAM has advantages such as low cost and low waste rate, it is advantageous compared to other AM methods based on laser and electron beams [12], making WAAM preferred in the production of many alloys. However, the WAAM method has some disadvantages, such as accuracy and surface roughness [7,8]. To date, aluminum alloys [13], low-high carbon steels [14], hot tool steel [15], stainless steels [5,6] titanium alloys [16], superalloys [17,18] and even high entropy alloys [19,20] and bi-metallic components [21] have been produced by WAAM method.

Stainless steels are widely used in various industries due to their high corrosion resistance and moderate mechanical properties [22–24], making them good candidates for WAAM [25]. In addition, studies have shown that the arc power to produce stainless steel is 5–10 ten times higher than those of laser powder bed fusion (L-PBF) and laser directed energy deposition (L-DED) processes. Thus, stainless steels structures can be fabricated in much shorter production time [25–28].

Many studies have been carried out on several aspects of the fabrication of stainless steels components by the WAAM method, including the chemical composition of the filler metals, process parameters, defects, residual stress and distortion, microstructure and mechanical properties. One of the critical issues that draw attention in these studies is the very high heat input caused by the WAAM process, which often affects the segregation of alloying elements and may cause undesirable meta-stable phase formations depending on the cooling process [5,6,25,26]. This further reduces the unsatisfactory wear resistance of stainless steel, even in traditional methods, such as casting, forging, etc.

Scientists have conducted many studies in order to solve this negative situation. For instance, Caballero et al. [29] found that shielding gases, which provide higher heat input during deposition, reduces the amount of residual austenite in the microstructure. The authors also reported that the mechanical properties of the samples, which were homogenized for 30 min at 1040 °C and aged for 1 h at 480 °C, were improved after homogenization, while they were deteriorated after the aging process due to the formation of harmful intermetallic phases. On the other hand, Wang et al. [5] investigated the effects of different arc modes on production process stability, structural integrity, and microstructure and mechanical properties of the fabricated components in the WAAM process at constant deposition rate. As a result, the authors reported that a component produced by the SpeedArc WAAM method has higher tensile strength and stiffness than a component produced by SpeedPulse WAAM due to its lower heat input and subsequent finer solidification structure.

In addition, 316 L stainless steel samples fabricated with WAAM were subjected to different heat treatments (i.e., 950 °C - 2 h, 1050 °C - 2 h, and 1200 °C - 1 h) by Rodrigues et al. [30] to understand the precipitation kinetics of secondary phases and to observe δ-ferrite dissolution behavior by synchrotron X-ray diffraction measurements. The authors observed that the microstructure of the as-built samples consisted of an austenite matrix (γ) and δ-ferrite dendritic structure. They also determined that the increase in the heat treatment temperature results in a decrease in the amount of δ-ferrite and hardness and reported direct relationship between the amount of delta ferrite and the hardness value. However, they did not study on the relationship between heat treatments and wear behavior. Zhang et al. [31] examined the unbalanced phase ratio and the effect of undesired secondary austenite structure on homogenization and corrosion resistance in duplex stainless-steel components manufactured with WAAM. They reported that the mechanical properties of the samples produced with WAAM after a heat treatment at 1300 °C for 1 h were comparable to hot rolled 2205 duplex stainless steel. They also proposed that the applied heat treatment process significantly improved the pitting corrosion resistance. The authors attributed the improvement in corrosion resistance to factors such as refining of crystals and microstructure, balanced phase ratio distribution, absence of chromium nitride, reduction of crystal defect density, and recrystallization of austenite after heat treatment.

The only study examining the high-temperature wear behavior of stainless steel structures fabricated by WAAM was carried out by Duraisamy et al. [32]. In their study, the authors compared the wear volume loss of 347 stainless steel structure produced with WAAM with wrought stainless steel at three different temperatures, namely 200, 400, and 600 °C. They observed that the component produced with WAAM had a heterogeneous structure. The hardness value decreased from the bottom section next to the substrate to the top region of the WAAM material. In addition, they determined that the wear resistance of the WAAM samples was lower than that of wrought 347 stainless steels. In addition, the authors noted that the volume loss of 347 stainless steel samples fabricated with WAAM was 13.0 %, 5.80 %, and 13.0 % higher at 200 °C, 400 °C, and 600 °C at 40 N load than wrought 347 stainless steel material, respectively. On the other hand, they reported that the volume loss of WAAM samples under 20 N load was 6.0 %, 29.1 % and, 208.0 % higher at 200 °C, 400 °C and 600 °C, respectively, compared to the 347 wrought materials. The authors attributed the inability to find a correlation between the wear temperature and wear rates to the heterogeneity of the samples produced with WAAM and to inhomogeneous oxide formation during wear.

Studies on the mechanical properties of WAAM-fabricated stainless-steel structures existing in the open literature have mainly focused on mechanical properties such as hardness and tensile strength [5,6,25,26,29–32]. These studies have shown in most cases that the mechanical properties of WAAM parts are somewhat lower than those of conventionally produced stainless steels [25,26,32], so their surface hardness need to be improved if they are used in abrasive environments.

Boriding is one of the methods applied to improve the wear resistance of stainless steel. Boriding, thermo-chemical surface modification method, is a heat treatment procedure based on the principle of diffusing boron atoms from a boron compound into the material at high temperatures and reacting with elements such as Fe, Cr, Ni, Ti, and Mo to form hard boride phases. Boriding not only increases the surface hardness of the metals, but also strengthens their lubrication performance [33–35]. This contributes to the superior wear resistance of ferrous and non-ferrous alloys in many environments such as air, water, various acid environments [36–38]. There are many studies in the literature on the improvement of wear resistance of stainless steels at room temperatures by the formation of complex hard boride layers containing NiB, CrB, NbB, and FeB [39–43]. In contrast, rarely study examined the high temperature wear resistance of borided stainless steels [44]. Moreover, no study on the boriding of stainless-steel structures produced by the WAAM method is present in the literature. However, parts with complex geometries can be easily boronized by powder-pack, liquid boriding and electrochemical boriding. Therefore, the boriding of samples with complex geometry produced with WAAM is also possible.

The ER307 wire is used *In the WAAM method, a metal wire is melted continuously* welds and can work harden rapidly under impact resistance [45]. In addition, the lower carbon content in its chemical composition minimizes deleterious carbide precipitation, providing good crack resistance and weldability between dissimilar steels. Therefore, in this study, the ER307 stainless-steel products fabricated by the WAAM method, which is becoming increasingly popular, were subjected to homogenization heat treatment and boriding process simultaneously at 1000 °C for 1 h to improve its wear resistance at room temperature and 500 °C. Furthermore, the effects of the applied heat treatment on microstructure, phase transformations, hardness and, wear behavior

were investigated in detail. This study is aimed to contribute to the literature about the boriding of WAAM samples and the effect of boriding on the wear behavior at high temperatures, which is a gap in the literature.

2. Materials and method

2.1. Gas metal arc welding-based additive manufacturing (GMAW-WAAM) process

307ER austenitic stainless steel wall structure of 5 mm thick, 50 mm in height, and 300 mm in length was fabricated on a 304 stainless steel substrate by the WAAM process. First, the substrate surface was cleaned with acetone to remove the grease or oil. Then, it was clamped to the working table to minimize the potential distortion due to the thermal input prior to the deposition process. A solid wire of ~ER307 (acc. to AWS A5.9) having a 1.2 mm diameter was used as filler metal, mainly used for moderate-strength welds with good crack resistance. The chemical composition of the wire employed (ER307) determined by XRF analysis is given in Table 1, together with the typical chemical composition of it according to AWS A5.9 standard. In contrast, the mechanical properties obtained by this wire are shown in Table 2. The GeKa-Tec WB 500 L welding machine with a water-cooled torch integrated on a 6-axis OTC Daihen D-V8L industrial welding robot was used as the power source of the WAAM system to produce austenitic stainless steel wall structure (Fig. 1). AWS A5.9 filler metal is named ER307 stainless steel after the WAAM fabrication process.

The certificated mechanical properties of the filler wire employed given in Table 2.

The deposition directions of two consecutive layers were reversed, and the first layer was deposited in the clockwise direction. It is known that the inter-layer cooling time directly influences the temperature distribution of the thin-walled components produced by WAAM [29]. Therefore, after the deposition of each layer, the torch was lifted by 1.7 mm. A waiting time of 120 s is employed to help the component transfer excessive heat to the environment (holding time for each layer to refine the previously deposited layer adequately). The temperature after each fifth layer before the deposition of the next layer was measured three times using the infrared thermometer. Three different measurements were performed, and their average was taken into consideration, and the results are shown in Table 3. It is seen that the interlayer temperatures increased with the increasing number of layers up to the 25th layer before becoming stable at around 185 °C. This is because the temperature gradient between the substrate metal and deposited layers is relatively large during the deposition of the first layers. Then the temperature gradient between the previously deposited layer and the newly deposited material decreases with the increased height. It means that the reduction in temperature due to the interlayer dwelling cannot compensate for the high heat input from the subsequent depositions. Thus, the heat exchange and cooling rate considerably decreased with increased deposited layers.

The WAAM component was built using a low spatter process with the following parameters: an arc current of 120 A, an arc voltage of 14.7 V, a scan rate of 50 cm/m, and a mixture of 97.5 % Ar and 2.5 % CO_2 gases as the shielding gas with the flow rate of 15 L/min. The contact tube-to-work piece distance was 13 mm. The main processing parameters involved in the deposition process are listed in Table 4. In addition, the inter-pass temperature is specified between 78 ± 5 °C and 186 ± 7 °C in AWS A5.4 to minimize the risk of solidification or liquation cracking for austenitic stainless steel filler metals. Thus, a waiting time of 120 s was employed between the layers to remove excessive heat of surface. The blade-like single wall component was fabricated by depositing thirty layers, each layer being about 300 mm in length, and 5 mm in thickness (Fig. 1). The chemical composition of the wall component was analyzed using an X-ray spectrometer (Rigaku ZSX Primus II), except carbon which was evaluated using a LECO C/S device. The average of XRF analyses conducted in nine locations in total, three measurements at each location namely, the root, center, and top regions, is given in Table 1.

Table 2
The certificated mechanical properties of the filler wire employed.

	Yield strength (MPa)	Ultimate tensile strength (MPa)	Elongation (%)	Charpy Impact Toughness (J at 20 °C)
ER307	432	646	35	105

The X-Ray inspection was conducted on the WAAM-produced wall according to EN ISO 17636-1 to detect whether any defects exist between the deposited layers (such as porosity, crack, insufficient melting, etc.). Following the X-ray testing, the metallography specimen and the specimens, which will be borided, were extracted using water cooled band saw machine. Microstructural characterization and hardness tests were performed on the metallography specimen, which was first subjected to standard metallographic preparation steps, i.e., grinding, polishing, and etching. Then, the polished specimen was electrochemically etched with 30 % HCI with a potential of 12 V for 5 min for the metallographic inspection to obtain the best phase contrast between the layers. The macroscopic evaluation was conducted using a Nikon SMZ745T stereo microscope, in accordance with following EN ISO 17639, to detect any solidification cracks or insufficient melting between the layers. Detailed microstructural investigations were performed using the Leica DMi8 optical microscope at root, center, and top regions along the building direction. The amount of delta-ferrite in the root, center and top regions along the building direction was volumetrically measured from five points for each region utilizing a Ferritescope (Fisher MP30) according to the magnetic induction method.

2.2. Boriding process

Since the samples produced by the WAAM process have a high surface roughness (R_a) of an average of 62.5 μm, the surface of the samples was subjected to CNC machining to reduce the surface roughness down to <3.25 μm. Following that, the surface of the samples was ground using 120–600 SiC sandpapers, and R_a values were reduced to <1 μm. Afterward, the samples were cut with a precision cutting device with the dimensions of 25 × 25 × 5 mm^3. Next, the residues on the surfaces were removed in an ultrasonic cleaner in ethyl alcohol for 15 min. The surfaces were finally cleaned with distilled water before boriding process.

The boriding process to be applied to the samples extracted from the wall structure produced by the WAAM process was chosen as 1 h at 1000 °C, based on the study in the literature [30], which reported to provide the most optimum results in the microstructure and mechanical properties of these steels. It has been stated that exposing WAAM

Table 1
Chemical composition (wt%) of the filler metal (ER307) used and standard ranges, as well as the average of the nine analyses conducted in three locations (lower, middle and upper part, three analyses at each location) of the deposited 307 austenitic stainless steel wall structure.

	C	Cr	Ni	Mo	Mn	Si	P	S	Cu	N (ppm)	Fe
Standard range for AWS A5.9	0.04–0.14	19.5–22	8.0–10.7	0.5–1.5	3.30–4.75	0.30–0.65	Max. 0.03	Max. 0.03	Max. 0.75	–	Balance
Filler metal	0.05	17.05	8.95	0.03	6.18	0.56	0.019	0.010	0.31	522	Balance
Deposited wall structure	0.04	16.97	8.11	0.03	4.96	0.58	0.023	0.017	0.20	567	Balance

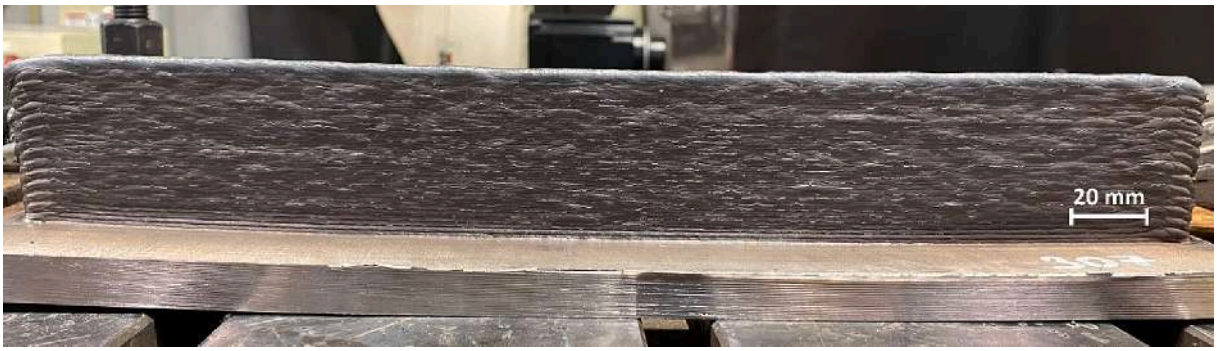

Fig. 1. Optical macrograph of ER307 austenitic stainless-steel wall structure fabricated by WAAM process.

Table 3
The temperature variation between each 5th layers.

Filler wire	5th layer (°C)	10th layer (°C)	15th layer (°C)	20th layer (°C)	25th layer (°C)	30th layer (°C)
ER 307	78 ± 5	105 ± 6	130 ± 8	166 ± 12	185 ± 10	186 ± 7

Table 4
Process parameters use in the WAAM process.

		ER 307
Current	A	120
Voltage	V	14.7
Travel speed	cm/min	50
Shielding gas		Ar 97.5 % + CO_2 2.5 %
Gas flow rate	l × min^{-1}	15
Contact tube to work piece	mm	13
Torch angle	°	Neutral (°)
Arc length	mm	5
Dwell time	seconds	120

austenitic stainless steel to long heating times at high temperatures may result in the formation of undesirable secondary phases in the microstructure of WAAM fabricated parts [30]. The boriding process was applied by keeping the samples embedded in 90 % B_4C + 10 % $NaBF_4$ powders in crucibles made of stainless-steel in an atmosphere-controlled furnace at 1000 °C for 1 h and then leaving the stainless-steel crucibles in the open air. Thus, the samples were subjected to both homogenization and boriding processes simultaneously [46].

As-built and borided samples were cut with a precision cutting device of 15 × 15 × 5 mm^3 for microstructural analysis. The cross-sectional surfaces of the samples were cold mounted and then grounded with 600–2500 SiC paper and polished by 1 μm diamond solution. Finally, the prepared samples were etched using 20 mL of HNO_3 and 80 mL of HCl with an etching duration of 15 s for microstructural detail. Thermo Fisher Scientific Apreo S LoVac SEM apparatus was used to perform SEM and EDS microstructure analyses of the polished samples utilizing a Circular Backscatter (CBS) detector, a 20 kV acceleration voltage, and a 10 mm spot size. XRD analyses were performed by evaluating the surfaces of the 20 × 20 × 5 mm as-built and borided samples. The XRD patterns were ascertained using computer controlled Panalytical Malvern Panalytical Empyrean (Netherlands) XRD equipment. Scanning parameters used in XRD analyzes were determined as: step size 0.0525211°, scan angle 2θ angles ranging from 10 to 90°, and Cu Kα radiation (1.5418 A°). Surface roughness values were calculated in a 2D profilometer (Hommelwerke T8000 GmbH, Germany) using 0.1 mm/s speed and 4.5 mm scan length parameters.

The hardness and elasticity modulus values of the samples were calculated by nanoindentation technique with Berkovich-tip. A Berkovich-tipped nano-indentation Hysitron TI-950 TriboIndenter (Germany) was used for the testing, which used a 10 mN load, a 30 s continuous loading rate, a 15 s dwell period, and a 30 s gradually unloading duration. The equations used to calculate nano-hardness and elasticity modulus can be reviewed from previous research by Oliver and Phar [47]. The nano-hardness and elasticity modulus values were calculated based on the average of at least five independent measurements. Tests such as nano-hardness, XRD, and abrasion were all performed based on the height (50 mm height) of the deposited WAAM layers.

Dry sliding ball-on disc wear tests were applied to compare the tribological behavior of the as-built and borided WAAM samples at room temperature and 500 °C. Wear tests were carried out using Turkyus POD&HT&WT, (Turkey) ball-on disc device with a high-temperature cell, based on a 10 N load, 100 mm/s (190.99 rpm) and, 100 m sliding distance against a 6.3 mm diameter WC-Co ball with a hardness of 19 GPa and a modulus of elasticity of 630 GPa.

The test parameter (100 m) chosen in the wear tests was determined as half of the boride layer thickness of 18 um, the depth of max shear stress on which the contact pressure values on the thin boride layers formed on the surface of the samples would affect. Thus, the wear process will be carried out on the boride layer. The corresponding values of maximum contact pressure, maximum shear stress, and contact radius were obtained via HertzWin software, which uses Hertzian stress equations to calculate contact parameters. The elastic modulus of the coatings was determined by nanoindentation measurements. The modulus of elasticity of the WC-Co abrasive ball is 630 GPa, and the Poisson ratio is 0.21 [48]. The values obtained as a result of the calculations are given in Table 5.

Young's modulus and Poisson ratio of the ball are 630 MPa and 0.21, respectively.

Young's modulus and Poisson ratio of FeB were taken as 310 and 0.25, respectively, from the literature [49].

Room temperature and 500 °C temperature values for wear testing were determined based on the usage areas of stainless steels and the temperatures at which they can be used alternatively to possible thixo casting molds made up of AISI H13 hot work tool steel [50]. The friction coefficients were automatically recorded based on the transmission of the data obtained by the load cell on the wear device to the TURKYUS

Table 5
Maximum contact pressure, maximum shear stress, and contact radius values obtained with HertzWin software.

Sample	Max. contact pressure (GPa)	Max. shear stress (MPa)	Depth of max. shear stress (μm)	Contact radius (μm)
As-built ER307	0.868	281.35	33.56	74.16
Borided ER307	2.762	901.55	18.81	41.58

software on the computer. In order to reduce standard deviations, each wear test was repeated three times. The depth and width of the wear marks formed on the surface of the worn samples were determined with a 2D profilometer, and the data obtained were calculated by putting them into the following equations, as stated in the previous study [51].

$$L = 2\pi r \tag{1}$$

$$V = 0.25\pi WD \tag{2}$$

$$W_r = \frac{V}{FS} \tag{3}$$

where L: Length of wear track (mm), V: Wear track volume (mm^3), r: Radius of wear track (mm), W: Average wear track width (μm), D: Average wear track depth (μm), F: Test load (N), S: Sliding distance (m) and W_r: Wear rate (mm^3/Nm).

Finally, SEM and EDS analysis were used to determine the wear mechanisms on the worn surfaces utilizing an Everhart–Thornley detector (ETD), a 20 kV acceleration voltage, and a 10 mm spot size.

3. Results and discussion

3.1. Microstructure, hardness and X-ray diffraction

The austenitic stainless steels solidify in four modes, including austenitic mode (A mode), austenitic-ferrite mode (AF mode), ferrite-austenitic mode (FA mode), and ferrite mode (F mode) [52]. The solidification mode is directly determined by the ratio between the chromium equivalent (Cr_{eq}) and nickel equivalent (Ni_{eq}). The Cr_{eq} and Ni_{eq} can be calculated by the Schaeffler formula, $Cr_{eq} = Cr + Mo + 1.5Si + 0.5Nb$ and $Ni_{eq} = Ni + 30C + 0.5Mn$ [53]. Based on the chemical composition of the deposited wall structure given in Table 1, the percentage of Ni_{eq} and Cr_{eq} is 11.79 % and 17.87 %, respectively; thereby the ratio of $Cr_{eq}/Ni_{eq} = 1.52$. When the ratio is changed from 1.48 to 1.95, the solidification mode becomes FA mode, and with the decrease in temperature, the solidification takes place as follows:

$$L \rightarrow L + \delta - \text{ferrite} \rightarrow L + \delta - \text{ferrite} + \text{austenite} \rightarrow \delta - \text{ferrite} + \text{austenite} \rightarrow \textit{austenite}$$

where the L defines the liquid [54]. Under equilibrium solidification conditions δ-ferrite is the leading phase, and austenite is the second phase that begins to form between the liquid and δ-ferrite dendrites in a peritectic reaction.

Fig. 2 reveals the microstructures of the as-built ER307 austenitic stainless steel wall structure in the root, center, and top regions of the building direction as well as in the interface of successive layers. Similar microstructures have different delta-ferrites along the austenite grain boundaries observed throughout the wall structure. However, the root region is mainly composed of a fine-grained structure due to the substrate's high cooling effect and heat dissipation during the layer depositions, as also pointed out by Yangfan et al. [55]. The reason for obtaining a similar microstructure throughout the wall structure from the bottom to the top region is the inter-pass cooling strategy used in the

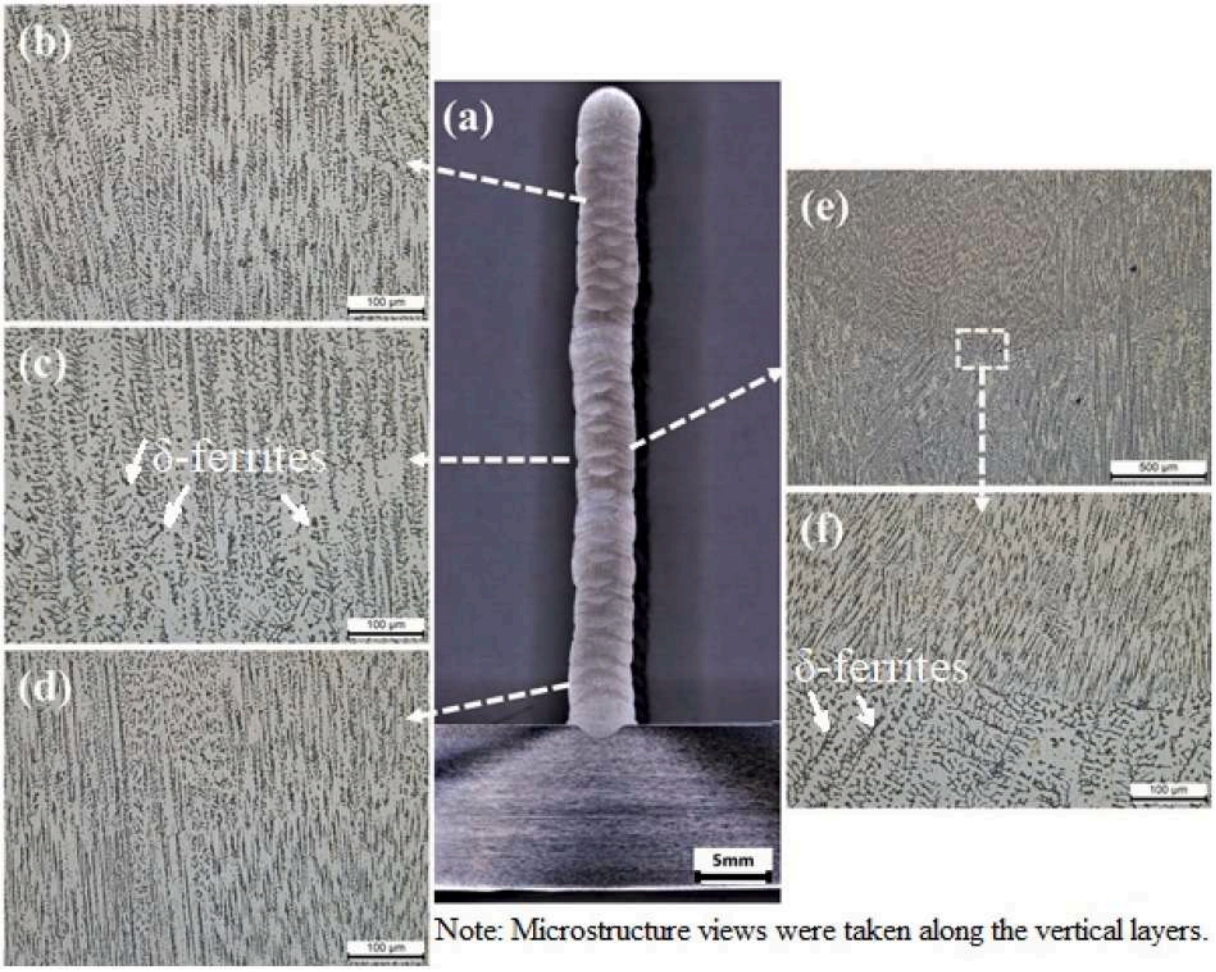

Fig. 2. Macrostructure a) and microstructures of the as-built ER307 stainless steel: b) top region, c) central region, and d) root region along the building direction, and e–f) interface of successive layers.

building process, which helped the transferring of the excessive heat to the environment and reduced the heat accumulation of the previously deposited layers.

As Fig. 2 shows, the residual δ-ferrites exist in the grain boundaries of austenite with skeletal and lathy morphologies. As the thermal cycle, the gradient of temperature and the rate of solidification are different in the root, center, and top regions of the wall structure and the amount, size, and the morphologies of the δ-ferrite change slightly along the building direction. The amount of residual ferrite was also measured with ferrite scope, and results were found as 3.5 ± 0.2 %, 3.2 ± 0.1 %, and 3.5 ± 0.1 % in the root, center, and top regions, respectively. The slight decrease in residual ferrite could be attributed to the dissolution of some of the primary ferrites into austenite due to the heat accumulation resulting from the previously deposited layers [56]. Moreover, Fig. 2e–f demonstrates that any specified layer in the middle region is characterized by finer columnar grains growing nearly vertically from the bottom of the layer and then transformed into coarse columnar structures with equiaxed grains in the top of the layer, as reported by Li et al. [57].

In Fig. 3, XRD patterns of as-built WAAM ER307 and borided WAAM ER307 samples are presented.

As seen in Fig. 3a, it was determined that the as-Arc DED fabricated ER307 sample consisted only strong diffraction peaks of γ iron-nickel-chromium based solid solution (Fe: 01-071-464961, Cr: 01-088-2323 and Ni: 01-077-8461) phase with face-centered cubic (FCC) crystal structure. γ peaks obtained correspond to 43.63° (111), 50.81° (200), 74.62° (220) degrees and planes and agree with previous studies produced with arc additive AISI 316 [30] and AISI 420 [58] structures. Therefore, XRD analysis did not exhibit delta ferrite in the structure. However, as discussed earlier, a small amount of delta ferrite (i.e., about 3 %) was measured with ferrite scope in the as-built structure. Apart from these phase formations, α-ferrite [59] and sigma phase formations [60] reported in the studies in the literature were not detected in the current study. This can be attributed to the very low amount of delta ferrite in the microstructure, i.e., about 3.5 % measured with ferrite scope, as mentioned earlier.

Considering Fig. 3b, it is seen that the phase structure has completely changed after boriding. After boriding, the dominant phase in the sample was FeB at the peak of 62.82° (020); however, it was determined that Fe_2B, Cr_5B_3, and MnB phases were also formed depending on the chemical content of the substrate. Since there is no study on the boriding of stainless steels produced with WAAM, the current study was compared with the studies on borided wrought austenitic stainless steels, and it was determined that the phase formations observed in the current study were similar to those obtained in boronized wrought stainless steels. For instance, Gunen et al. [43,61,62] reported that FeB is the dominant phase in borided wrought AISI 304 stainless steels, as well as Fe_2B, CrB, NiB, and MnB phase formations. Similarly, Gunes and Yildiz [43] determined FeB, Fe_2B, CrB, Cr_2B, NiB, Ni_2B, and Ni_3B phases on AISI 310 stainless steel. Kayali et al. [63] also reported FeB, Fe_2B, CrB, Cr_2B, NiB, and Ni_2B phase formation on borided AISI 316 stainless steel.

Fig. 4 gives the SEM micrographs showing the microstructure of the as-built WAAM ER307 stainless steel wall structure and the EDS analysis results conducted. The longitudinal cross-sectional view as-built Arc DED ER307 specimen is illustrated in Fig. 4a. The macrostructure of the as-built specimen displayed a layered appearance, as thirty layers were deposited in the additive manufacturing of the samples, the thickness of each layer was in the range of 1.2–1.8 mm (ave. 1.65 mm). The detailed microstructural investigations clearly showed no defects, such as inter-layer cracks or pores in the transition region between the base layer and

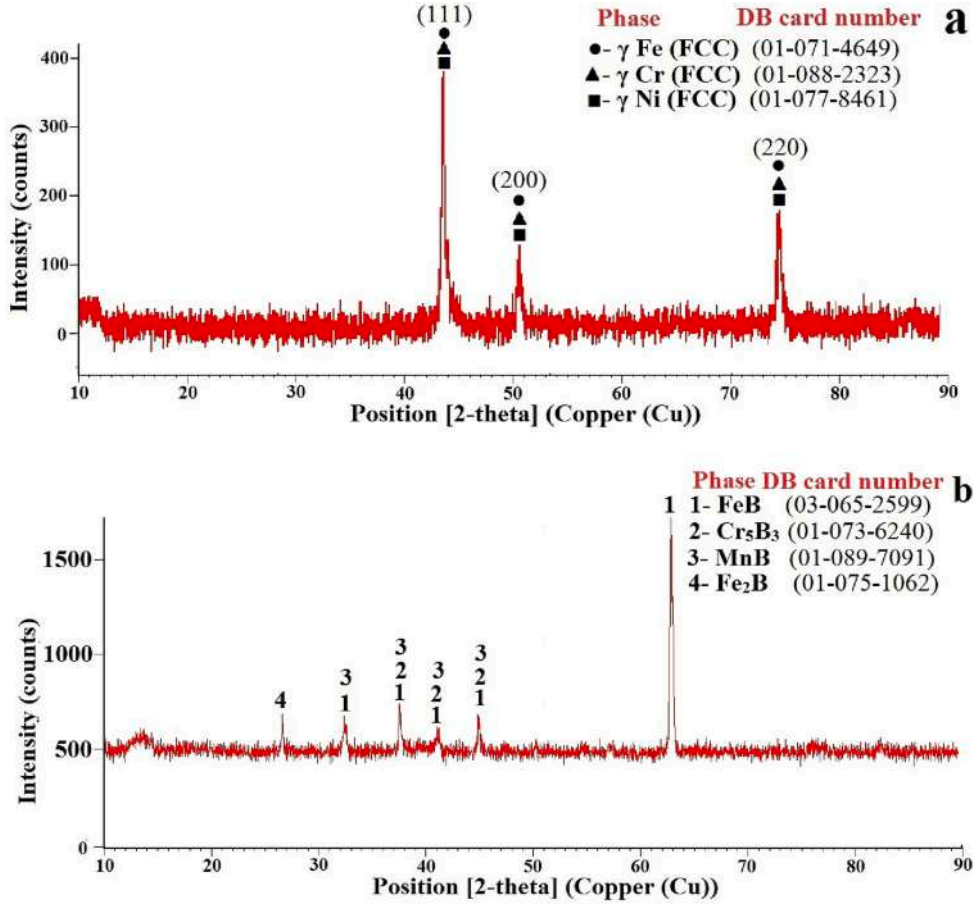

Fig. 3. XRD patterns obtained on the surface of a) as-built Arc DED ER307 and b) borided Arc DED ER307 samples.

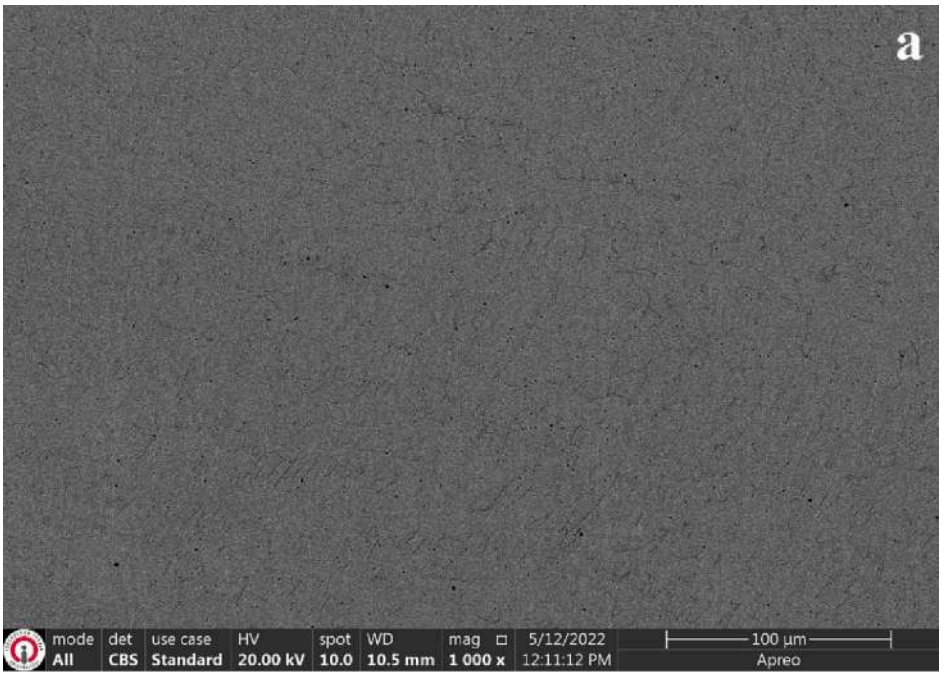

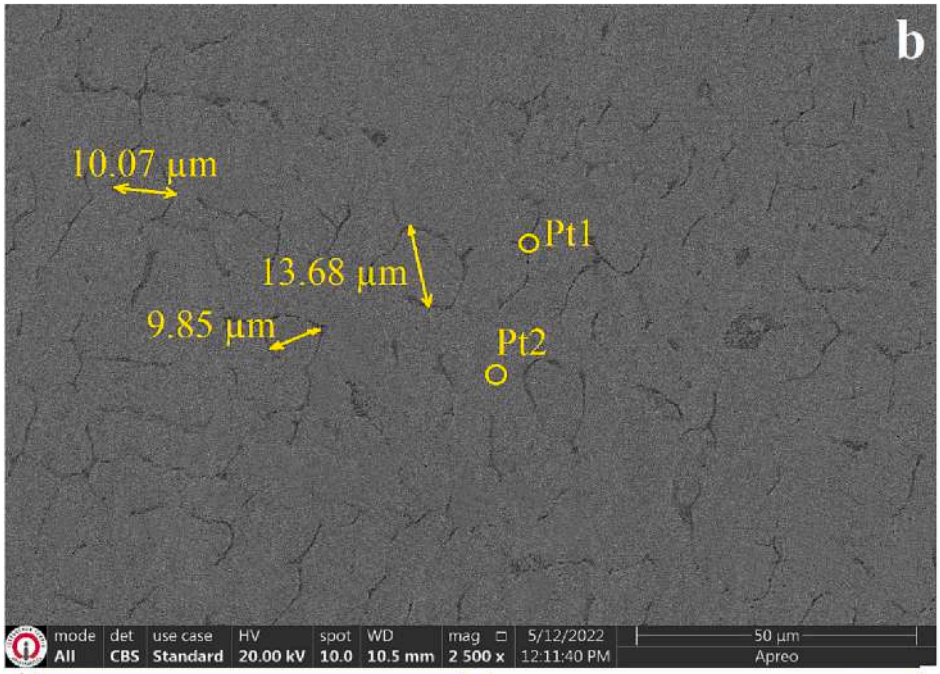

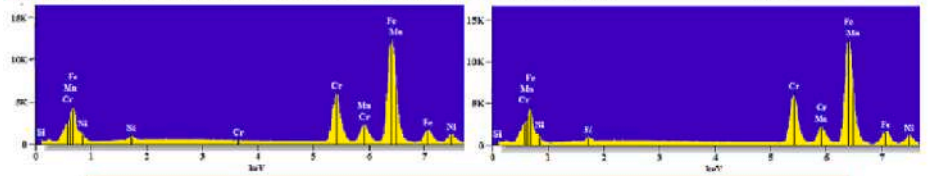

Wt. %	Si-K	Cr-K	Mn-K	Fe-K	Ni-K
Pt1	0.68	19.61	6.14	66.19	7.38
Pt2	0.69	19.70	6.22	66.08	7.32

Fig. 4. Cross-section SEM micrographs of the as built WAAM ER307 stainless steel and the results of the EDS analyses conducted at different locations a) 1000× b) 2500×.

the substrate. In addition, a microstructure with a grain size of 11.3 ± 1.6 μm with an appearance resembling dendritic and interdendritic structures was observed as shown in SEM in Fig. 4b. As can be seen from the higher magnification SEM micrographs given in Fig. 4b, the dendritic and interdendritic regions have a homogeneous distribution in every part of the sample. The chemical compositions conducted at different positions (Pt1 and Pt2 in Fig. 4b) are very close to each other, so it can be said that the samples produced with WAAM have a homogeneous elemental distribution.

The microstructural SEM section view of borided WAAM ER307 wall structure is shown in Fig. 5.

Considering Fig. 5, 4 different regions on the surface is seen. These regions are (i) 20.10 μm thick FeB layer, (ii) 8.52 μm thick Fe_2B layer, (iii) 14.25 μm transition zone, and (iv) the substrate region where the diffusion of boron does not reach. Microstructure interpretations in the literature report that the upper part of the boride layer, which has a

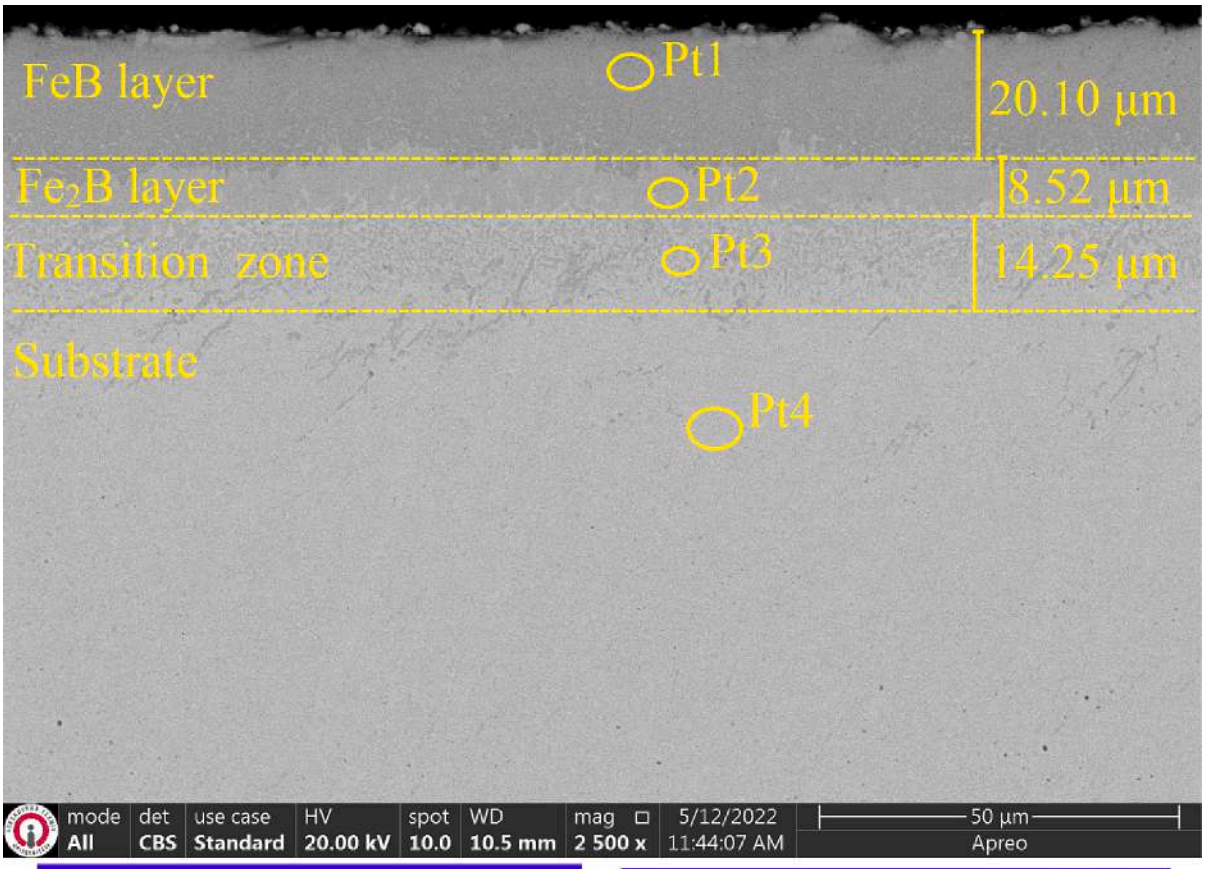

Wt.%	B-K	C-K	Si-K	Cr-K	Mn-K	Fe-K	Ni-K
pt1	30.49	0.00	0.06	14.61	4.51	47.87	2.46
pt2	27.11	0.00	0.74	14.30	5.19	46.32	6.34
pt3	23.41	0.00	0.93	15.73	5.00	48.81	6.12
pt4	0.00	5.75	0.62	18.50	5.48	63.72	5.93

Fig. 5. SEM cross-section view of the borided WAAM ER307 stainless steel wall structure.

darker contrast, is the FeB layer, and the lighter secondary layer is the Fe_2B phase [39,41,64]. In addition, the microhardness values taken from these regions confirmed this determination (Table 6). Although there was no boron diffusion to the region (iv), it was determined that the interdendritic structures that appeared in the as-built structure disappeared. Thus the structure attained a homogeneous appearance. This situation can be attributed to the fact that the sample was subjected to the boriding process at 1000 °C for 1 h and then left to cool in an open-air environment. This process, in addition to forming a boride layer on the surface of the specimen, also provides an effect as if the material has been subjected to homogenization heat treatment at the same time as stated in the previous study conducted on heat-treated WAAM Inconel 625 [29,30]. Considering the boride layers formed on the surface, it has been determined that the formed boride layer has a flat-uniform structure as in wrought stainless steels and in dual-phase (FeB + Fe_2B) structure [39,40,64,65]; however, it does not contain any flaws such as cracks, porosity and, discontinuity. The dual-phase formation is not desirable in borided steels, and stainless steels [66–68], especially in applications where wear resistance is important [43]. Because FeB and Fe_2B have different thermal expansion coefficients, they inevitably exhibit different cooling behaviors during cooling, which often causes cracks between FeB and Fe_2B phases. As seen in Fig. 5, no cracks were observed in the boride layer. This is a result of the low thickness values of the FeB and Fe_2B layers due to the low boriding time. In the literature, it has been reported in many studies that an increase in FeB and Fe_2B layers occurs as a result of longer boriding of stainless steels, and cracks occur during cooling due to the different expansion coefficients of FeB and Fe_2B layers [39,40,64,65]. As a matter of fact, the formation of a diffusion zone between the coating layer and the as-built matrix in thermochemical coatings increases the adhesion force between the coating layer and the substrate [69,70]. When the EDS analysis of the Pt1 region in Fig. 5 was examined, it was determined that the formed boride layer (i.e. FeB) had approximately 30 % boron content. Moreover, the boron content showed a decrease from the surface to the substrate, and the boron reached 0 % value in the Pt4 as-built matrix region.

The surface condition of the boride layer is as important as the cross-sectional area. Because the first contact takes place via the surface in the conditions of wear, corrosion, etc. SEM micrograph showing the surface microstructure of ER307samples produced with WAAM and then borided and EDS analyses results conducted at three locations are presented in Fig. 6.

When the surface of boride coating is studied (Fig. 6), it is seen that the majority of the surface is made up of angular-shaped grains measuring 3–4 μm and pits stuck in between these grains measuring 0,5–1 μm (Fig. 6a). Pit forms were more easily seen when the microstructure of this SEM picture was examined in detail (Fig. 6b). In the EDS analyses taken from the grains (Pt1 and Pt3), the presence of boron around 31–36 % by weight was determined in accordance with the cross-sectional views of the borided samples. On the other hand, the EDS analysis taken from the pits region (Pt2) showed that the boron ratio was around 50 % and these pit regions contained higher O_2 (7.07 %) than the grain interiors. This situation can be attributed to the boriding powders trapped in the pits. The grain and pits structure formed on the surface of the samples are related to the crystal structure of the boride phase, which changes depending on the boron metal ratio in the structure of the boride coatings. Zhao et al. [71] reported that changes in the B/M ratio reveal domains with diverse and broad phase stability whose structures are largely based on close packing of metal atoms with boron atoms filling octahedral spaces. Therefore, it causes these structures to exhibit a complex structure depending on the mixture of bonds between metals such as Fe, Cr, Ni and boron atoms. Consequently, in mixed-phase areas, existing multiphase phase formations often precipitate or magnify certain morphologies, forming the microstructure.

Microhardness and modulus of elasticity values of as-built and as-built + borided samples are given in Table 6. As can be seen from Table 6, the hardness and modulus of elasticity of the WAAM ER307 sample, which was used as the substrate material and normalized during the boriding process, were determined to be 2.96 ± 0.3 and 130.32 ± 2.75 GPa, respectively. The hardness value of as-built material is similar to those of additively manufactured austenitic stainless steels reported in the literature [5,24,25,29]. On the other hand, the hardness value of the borided sample is 21.45 ± 3.75 GPa and 17.80 ± 1.2 GPa for the FeB and Fe_2B regions, respectively, while the elasticity modulus is 310 ± 35 GPa and 245 ± 24 GPa for the FeB and Fe_2B regions, respectively, which is consistent with the studies published in the literature on steels. [49,72]. While the surface roughness values of the samples were 0.75 ± 0.06 in the samples ground with 600 SiC paper, it was determined that the surface roughness values of the samples after boriding decreased to 0.42 ± 0.05 μm. Şahin [73] and Krelling et al. [74] stated that if the surface roughness value before boriding is below the threshold value, there will be an increase in the surface roughness values after boriding. In the opposite case, they reported that the roughness values would decrease compared to before boriding. Therefore, the fact that the Ra value of 0.75 before boriding decreased to 0.42 um in the study indicates that the surface roughness values of the samples before boriding are above the threshold value.

3.2. Friction and wear behavior

The friction coefficient courses (COFs) of the as-built ER307 and built + boronized ER307 samples against the WC-Co ball at room temperature and 500 °C are shown in Fig. 7.

As seen from Fig. 7, in the wear tests carried out at room temperature, the friction coefficient of the as-built sample (as-built- 25 °C) was 0.2 at the beginning of the test and reached around 0.6 with a continuous increase until the sliding distance of 30 m, and then a near-stable friction coefficient course was observed in the range of 30–100 m sliding distance. In the wear test of the borided sample, although a lower friction coefficient course was observed compared to the as-built sample, but the friction coefficient reached a stable course only after the sliding distance of 80 m. This is due to the fact that the surface roughness caused by the height difference between the grains on the surface and the pits continues up to this sliding distance, as can be seen in the

Table 6
Surface roughness, boride layer thickness and nanohardness of the samples.

Sample	R_a (μm)	Built thickness (mm)	Nanohardness	
			As-built hardness (GPa)	As-built elasticity modulus (GPa)
As-built ER307	0.75 ± 0.06	150 mm	2.96 ± 0.3	130.32 ± 2.75

Sample	R_a (μm)	Boride layer thickness (μm)	FeB layer (GPa)	FeB layer elasticity modulus (GPa)	Fe_2B layer (GPa)	Fe_2B layer elasticity modulus (GPa)
Borided WAAM ER307	0.42 ± 0.05	35 ± 2.3	21.45 ± 3.75	310 ± 35	17.80 ± 1.2	245.0 ± 24

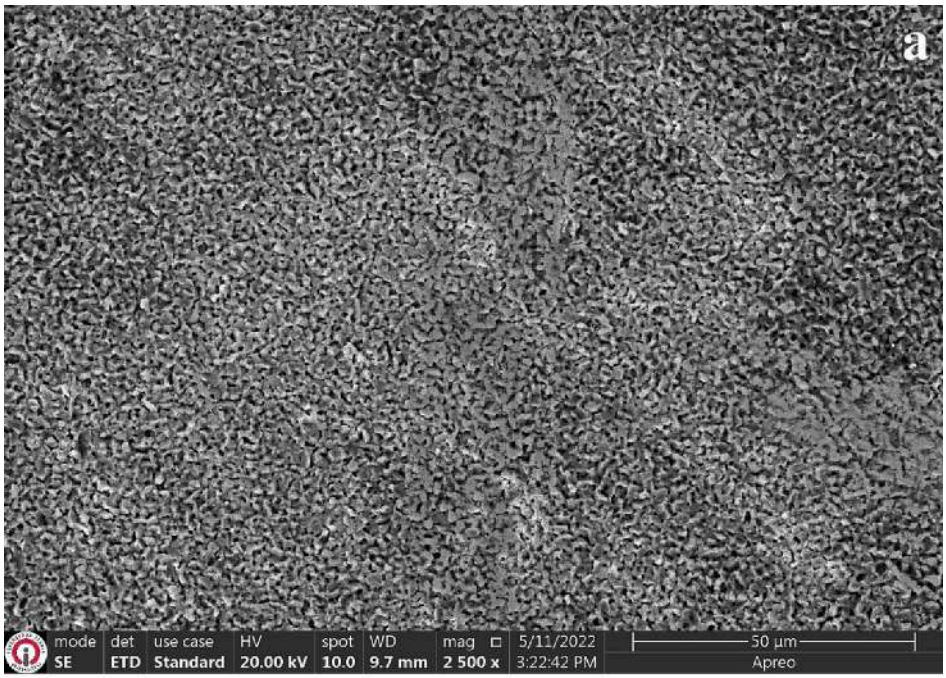

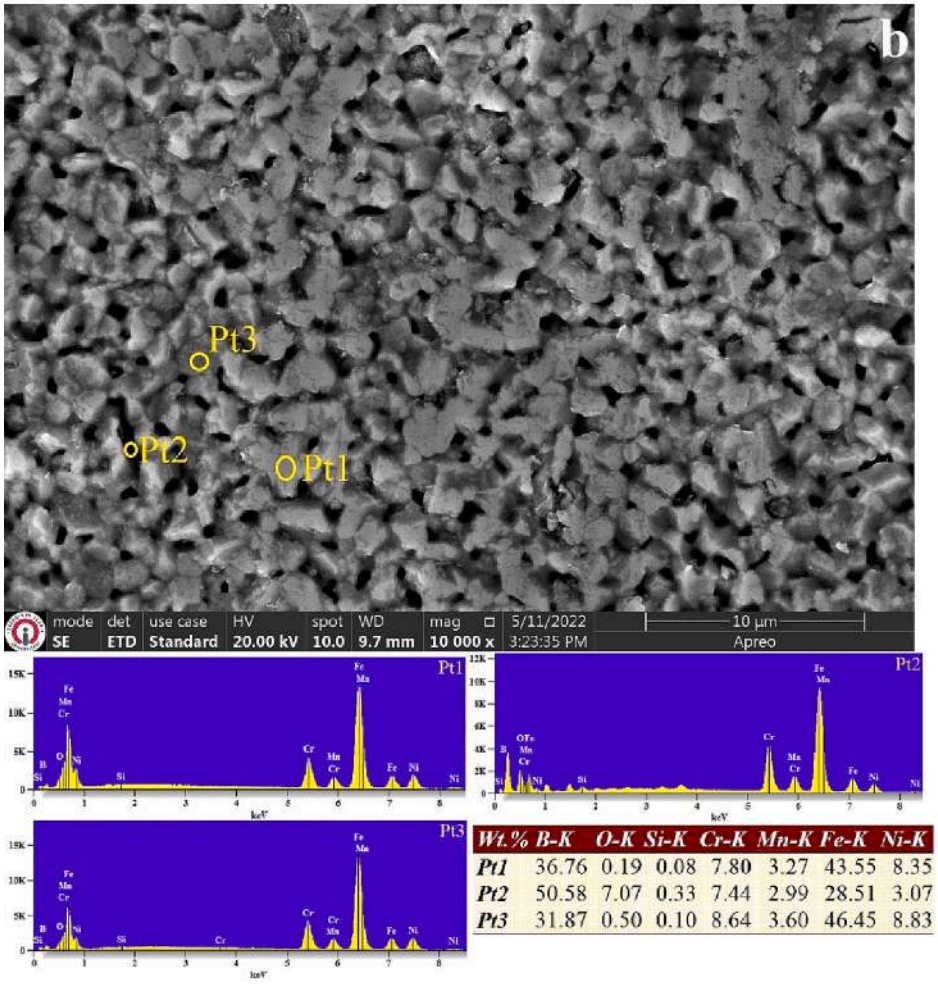

Wt.%	B-K	O-K	Si-K	Cr-K	Mn-K	Fe-K	Ni-K
Pt1	36.76	0.19	0.08	7.80	3.27	43.55	8.35
Pt2	50.58	7.07	0.33	7.44	2.99	28.51	3.07
Pt3	31.87	0.50	0.10	8.64	3.60	46.45	8.83

Fig. 6. SEM surface micrograph of the WAAM borided ER307 stainless steel wall structure and EDS analyses results a) 2500× b) 10,000×.

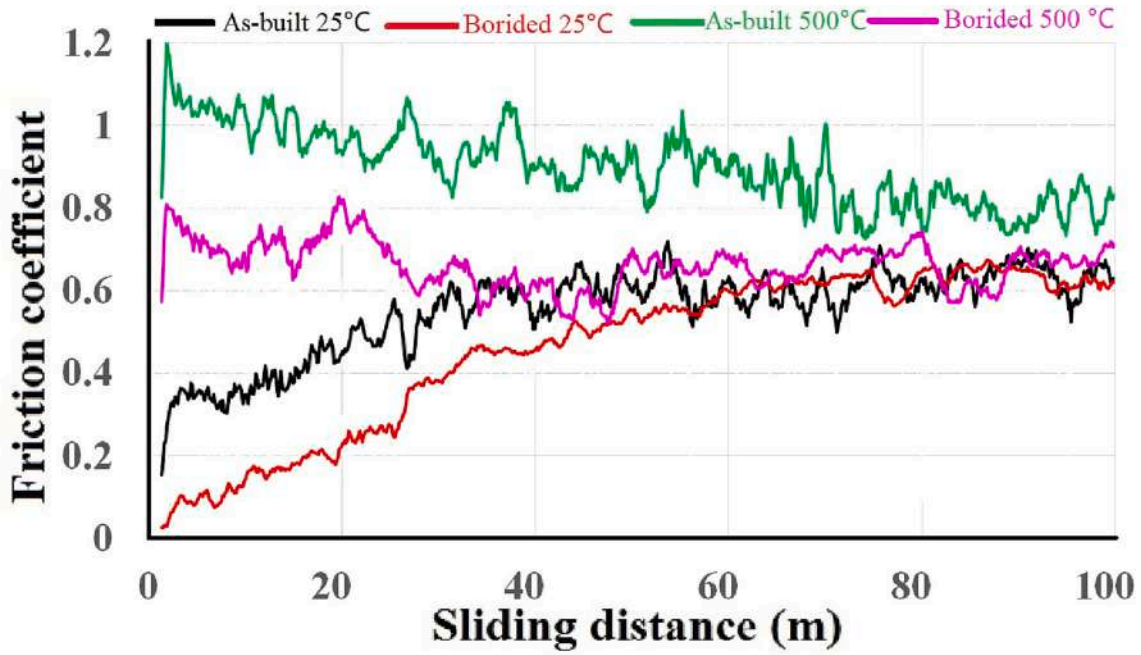

Fig. 7. COF graphs were obtained as the articulation against WC-Co ball at room temperature and 500 °C.

micrograph showing the surface microstructure given in Fig. 6. Generally, high coefficient of friction values seen as a result of the wear test also indicate high wear losses. A high coefficient of friction means that the abrasive tip is more difficult to move over the sample surface. This results in a greater impact of the abrasive tip on the sample surface. Therefore, the resulting deformation increases and wear losses increase. To overcome this situation, lubricants are mostly used to reduce friction between two surfaces. When the graphs of friction coefficients at high temperature are examined, it is seen that both as-built and borided samples exhibit a higher friction coefficient compared to room temperature. In the high temperature friction coefficient graphs, it is clearly seen that the borided sample follows a lower friction coefficient course than the non-borided sample, as the case at room temperature. The lower coefficient of friction of the borided sample at both room and high temperatures has also been reported in many previous studies, and this can be attributed to the resistance of the boride layers to plastic deformation [75,76] due to high hardness as well as the self-lubrication property of the boride layers [33–35]. On the other hand, the friction coefficients of boronized and non-boronized samples are higher at high temperatures than at room temperature. This may be caused by the decrease in the mechanical properties of the as-built matrix and coatings due to the high temperature effect and the breakage of the oxidation layer due to the increase in temperature and excessive increase in the oxidation layer thickness. Ultimately, higher coefficients of friction are compatible with higher wear volume losses. [32,66,76].

Table 7
Data obtained as a result of the ball-on-disc wear tests.

Nomenclature	Wear temp. (°C)	Mean COF	Wear track width (μm)	Wear track depth (μm)	Wear rate (10^{-5} mm^3/Nm)
As-built	25	0.55 ± 0.02	851.4 ± 23	20.43 ± 0.6	40.99 ± 2.7
Borided		0.46 ± 0.19	261.89 ± 14	2.10 ± 0.36	1.29 ± 0.04
As-built	500	0.90 ± 0.25	2065.68 ± 48	24.33 ± 1.3	118.34 ± 4,7
Borided		0.79 ± 0.12	1246.01 ± 46	5.01 ± 0.24	14.72 ± 0.05

Table 7 gives the wear track widths and wear track depths determined on the surface of as-built and boronized WAAM ER307 stainless steels by the room temperature and 500 °C temperature dry sliding wear behavior analyses and the calculated wear track volume and wear rates from these test results. As the abrasive tip moves on the sample surface, it causes deformation on the opposite surface with the effect of the load. Depending on the mechanical properties of the material, the part is usually removed from the opposite surface during this deformation. Due to the spherical shape of the abrasive tip, the trace on the sample surface both deepens and widens as the wear test continues. The width and depth of the trace actually gives information about the wear resistance of that material as well. A deep and wide track indicates low wear resistance, while a shallow and narrow track indicates high wear resistance [77].

It can be seen from Table 7 that the wear track widths and depths observed on the surface of the as-built sample after both room temperature and 500 °C wear tests were higher, thus more wear damage occurred, and this is consistent with the graphs of friction coefficient. The improvement in the room temperature wear resistance of the boronized samples is the result of the increase in the hardness values of the as-built sample in the range of 7–8 times after boriding and the higher modulus of elasticity obtained after the boriding process compared to the as-built samples. Because the higher hardness and elasticity modulus of the samples means that these samples show higher resistance to plastic deformation. As a matter of fact, boronized samples showed a wear resistance 31.78 times better than the as-built sample at room temperature. This is the case where the mass loss is inversely proportional to the hardness of the material according to Archard's wear law, and it has also been reported in the studies performed by Li et al. [78] and Reséndiz-Calderon et al. [79] on boronized stainless steels. On the other hand, at high temperature, it was observed that the boronized sample exhibited a wear resistance 8.04 times better than the as-built sample, the improvement being lower compared to that in room temperature. This increase in wear resistance at high temperatures can be attributed to maintaining the presence of boride layers up to 1050 °C. [44,50]. On the other hand, the higher volume losses of the boride layers compared to room temperature are the result of the moderate oxidation resistance of the boride layers at high temperatures [80].

In addition to the friction coefficient and wear volume losses of the

materials, the characterization of the worn surfaces is extremely important in terms of determining the wear behavior of the materials. For this purpose, wear tracks were examined by SEM and EDS analyses were carried out in the regions where necessary. The eroded surface morphologies of the samples subjected to ball-on disc abrasion test at room temperature are shown in Figs. 8 and 9.

As seen in the wear track line SEM micrograph of the as-built sample taken at 200× magnification (Fig. 8a), it is clearly seen that deep grooving occurred on the surface of the sample parallel to the wear direction and delaminations caused by plastic deformation in some regions. Moreover, micro-grooving, micro-crack, delamination and abrasion residues are also clearly seen in a larger magnification SEM micrograph of the specimen (Fig. 8b).

Such wear mechanisms are the wear types observed in WAAM stainless steels [32], wrought stainless steels [81] and Ni-based superalloys [82,83], which are known for their low surface hardness. Birol [82] states that during the wear of materials with low surface hardness, continuous sliding causes shear stresses on the abraded surfaces, and shear stresses cause plastic deformation after a certain stage producing plate-like parts on the surface and subsequently producing plate-like morphology over and over again leading to the existence of wear residues and irregular regions. Therefore, it was concluded that the wear mechanisms observed in the as-built samples are micro grooving, deep grooves, abrasive and severe plastic deformation. These findings are in agreement with the coefficient of friction plots. Because the high friction force causes high plastic deformation and therefore serious damage to the materials. In the EDS analyses conducted in various locations on surface the samples, it was observed that the as-built samples had a chemical composition close to each other on the entire surface. Therefore, it was determined from the observed wear morphologies that abrasive and plastic deformation were more dominant than other mechanisms on the worn surfaces, and this is in good agreement with the findings of Duraisamy et al. [32] and Bahshwan et al. [84] in additively manufactured stainless steels.

When the wear track appearance of the boronized sample was examined (Fig. 9a), a smoother surface and a much narrower (one third) abrasion track formation were observed compared to the as-built samples. The narrower wear marks are supported by the data in Table 7. When the worn surface SEM micrographs in Fig. 9b are examined, it is seen that a structure similar to the pits and grain formations in the SEM pictures taken from the surface in Fig. 6b is seen, but lateral cracks and vertical cracks have formed in the boride layer due to the effect of the abrasion process. Although the pit formations have decreased, their existence supports the fact that the stable range in the friction coefficient at 80 m has been reached. This is the result of the 10 N load applied to the hard boride layer in the samples, resulting in micro-cracks on the surface due to the repeated loads applied as a result of the abrasive ball not being able to penetrate the hard surface easily. These cracks are caused by the fact that FeB layer causes tensile stress in the boride layer formed on the surface, while the Fe_2B layer causes compressive stress [85–87]. Because with the force applied to the surface, a hertz shear stress is applied on the boride layer, which is formed perpendicular to the surface due to a tensile stress produced along the contact periphery of the near-surface borides and provides the formation of lateral and perpendicular cracks in the microstructure [48,88,89].

Side cracks are horizontal cracks that form below the surface and are symmetrically concerning the load axis. Lateral cracks are produced by tensile stress and may extend to the surface as a surface ring which can cause the surface to crumble from the sample. As seen in Table 7, the depth of maximum shear stress is 18.81 μm for the boronized sample, and its effect is limited to the 20 μm FeB layer. EDS analysis determined that the lateral and perpendicular cracks in the erosion process are not destructive (they do not tear the boride layer from the surface).The detection of 41.22 % (Pt1) and 36.72 (Pt3) boron by weight in the EDS analyses taken on the worn surfaces shows that the boride layer remains on the as-built matrix after the abrasion process. In the region with wear debris (Pt2), the boron ratio is 29.22. Therefore, the wear mechanism of the boronized sample was considered to be polishing type wear supported by micro-crack.

SEM images of the wear tracks of the samples after the wear tests of as-built and boronized WAAM fabricated ER307 stainless steel specimens at 500 °C are shown in Figs. 10 and 11.

When Fig. 10 is examined, it is seen that the wear track is approximately 2.5 times wider than the room temperature. This is because, as a result of the softening of the sample exposed to 500 °C, the abrasive ball sinks deeper into the surface with the applied load and causes easier wear due to the less resistance of the softened surface. When the wear track is examined in detail, it is seen that there is a smoother surface, in contrast to the room temperature wear, and it is seen that the surface consists of oxidation layer and extruded regions that undergo plastic deformation. The presence of an oxidation on worn surfaces is due to friction heating at higher ambient temperatures [32,90]. As seen in the analyses carried out, the detection of oxygen in the range of 23.3–24.7 % on the surface of the samples supports the existence of an oxidative-supported plastic deformation mechanism of the surface. On the other hand, smooth surfaces are the result from the application of sufficient contact pressure at high temperatures, and subsequently acting of the glazed layer, which adheres to the as-built matrix with good adhesion as an intermediate protective layer between the abrasive ball and the as-built material [91]. The wear behavior of as-built samples at high temperatures is consistent with the findings of Duraisamy et al. [32] in the wear behavior of WAAM stainless steel at 600 °C. In tests carried out at 500 °C, the oxidation rate becomes much higher than at room temperature due to heat, sufficient air in the environment, and the formation of an oxide layer on the material. It was concluded that this upper layer comprised of iron oxide and chromium oxide since high levels of Fe, Cr, and oxygen was detected in the EDS analyses. Duraisamy et al. [32] reported that the oxidative layer of WAAM stainless steel at 200, 400, and 600 °C consists of Fe_2O_3 and Fe_3O_4 but did not mention chromium oxide.

SEM image of wear track and EDS analysis results of borided WAAM ER307 sample are given in Fig. 11.

Although the surface appearance of the boronized sample after the wear process at 500 °C exhibits a wider wear track width than the room temperature, the wear track formed is 60 % of the wear track in the as-built sample. Contrary to room temperature, it is seen that the surface is not entirely smooth, and the coating layer is lifted from place to place. This explains the decrease in the wear resistance of the boronized samples at high temperatures to around 8 times, which is around 31 times at room temperature. The formation of a wider wear trace than room temperature in the boride coating is due to the decrease in the hardness values of the boride coating with the effect of high temperature and the oxidation effect. Considering that the contact pressure acting on the boronized samples was 2.76 GPa (Table 5), it was evaluated that the oxidative supported delamination wear mechanism occurred.

Wang et al. [92] stated that the oxidative-assisted wear mechanism may occur as a slight oxidative wear, oxidative fatigue delamination, abrasion wear and oxidative wear mechanism depending on the oxidation of steels under atmospheric conditions and the contact pressure values acting on their surfaces. In this context, they proposed that while oxidative fatigue delamination and a mild oxidative wear mechanism occur if the contact pressure values are below 3.54 MPa, oxidative wear, oxide fatigue delamination, and oxidative delamination wear will occur in the range of 3.54–5.31 MPa, and oxidative delamination wear and severe wear as a result of plastic extrusion will dominate when it exceeds 5.31 MPa. On the other hand, this non-smooth surface friction coefficient at high temperatures caused the graphs to be more zig-zag compared to room temperature.

Therefore, as seen in Table 5, considering the contact pressure of 2.76 GPa in borided samples, it has been determined that oxidative supported fatigue delamination wear mechanisms occur in borided WAAM samples at 500 °C. Furthermore, as seen in the EDS image, lower

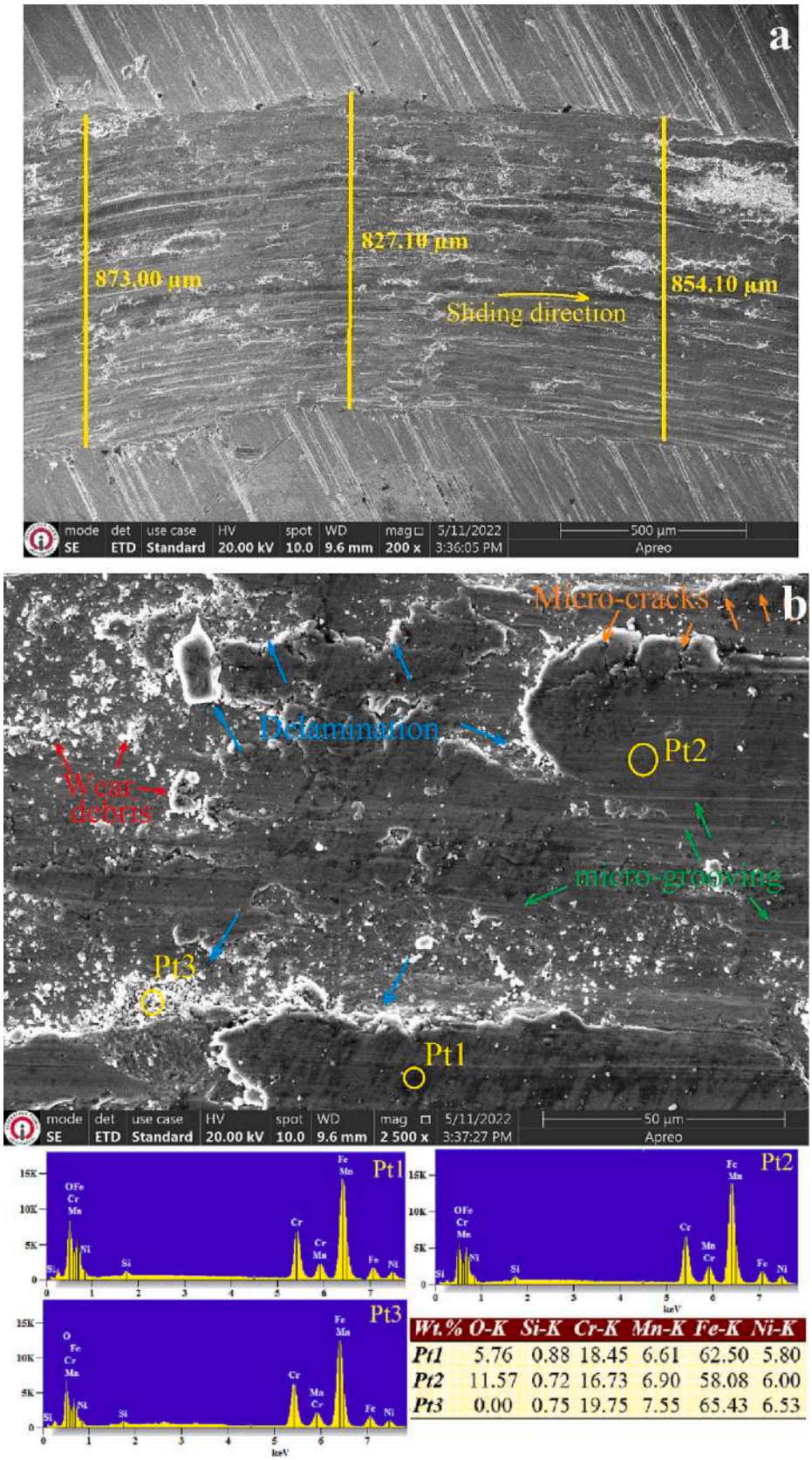

Wt.%	O-K	Si-K	Cr-K	Mn-K	Fe-K	Ni-K
Pt1	5.76	0.88	18.45	6.61	62.50	5.80
Pt2	11.57	0.72	16.73	6.90	58.08	6.00
Pt3	0.00	0.75	19.75	7.55	65.43	6.53

Fig. 8. SEM surface micrograph and results of EDS point analyses conducted on the worn surface of as-built WAAM ER307 stainless steel to wear testing at room temperature a) 200× b) 2500×.

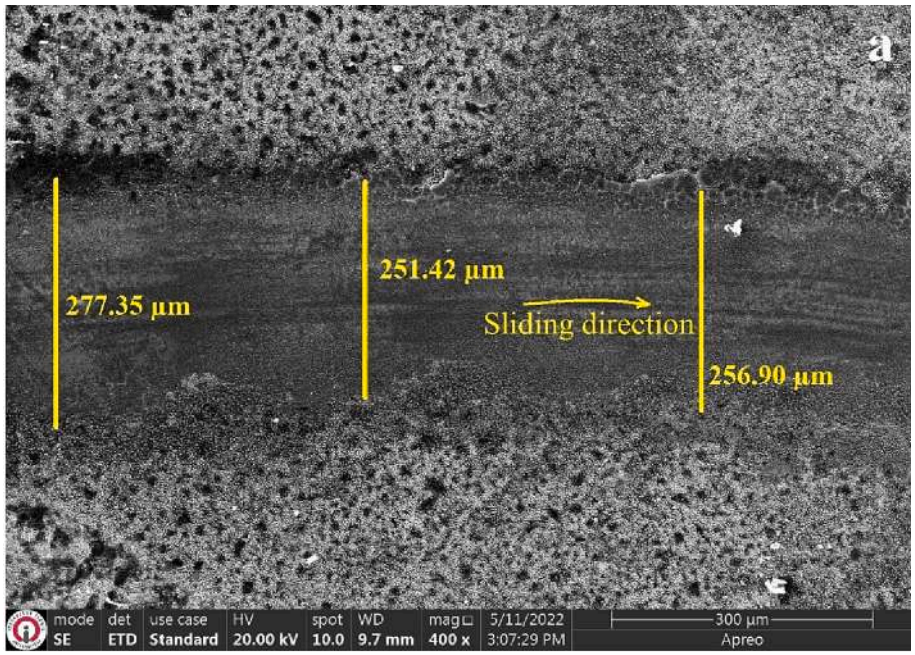

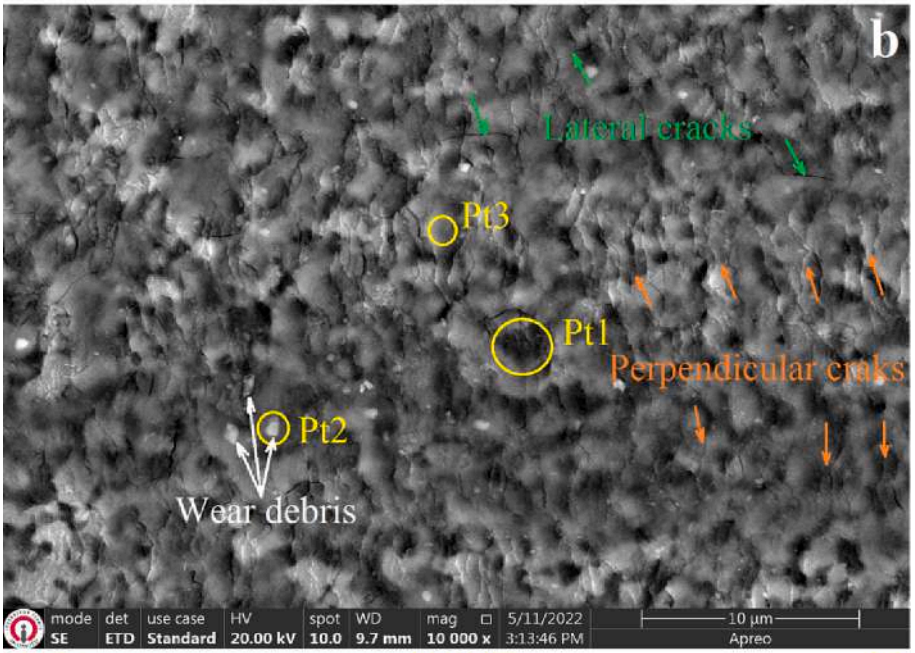

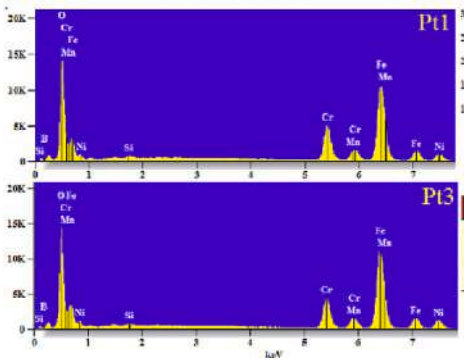

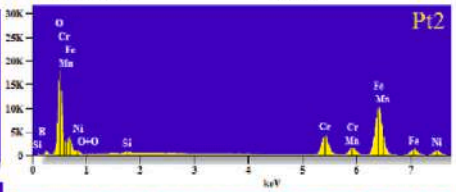

Wt.%	B-K	O-K	Si-K	Cr-K	Mn-K	Fe-K	Ni-K
Pt1	41.22	0.00	0.32	10.82	3.59	39.00	5.06
Pt2	29.22	16.99	0.30	9.31	3.19	36.15	4.83
Pt3	36.72	0.00	0.34	10.04	3.55	43.01	6.34

Fig. 9. SEM surface micrograph and results of EDS point analyses conducted on the worn surface of borided WAAM ER307 stainless steel exposed to wear testing at room temperature a) 400× b) 10,000×.

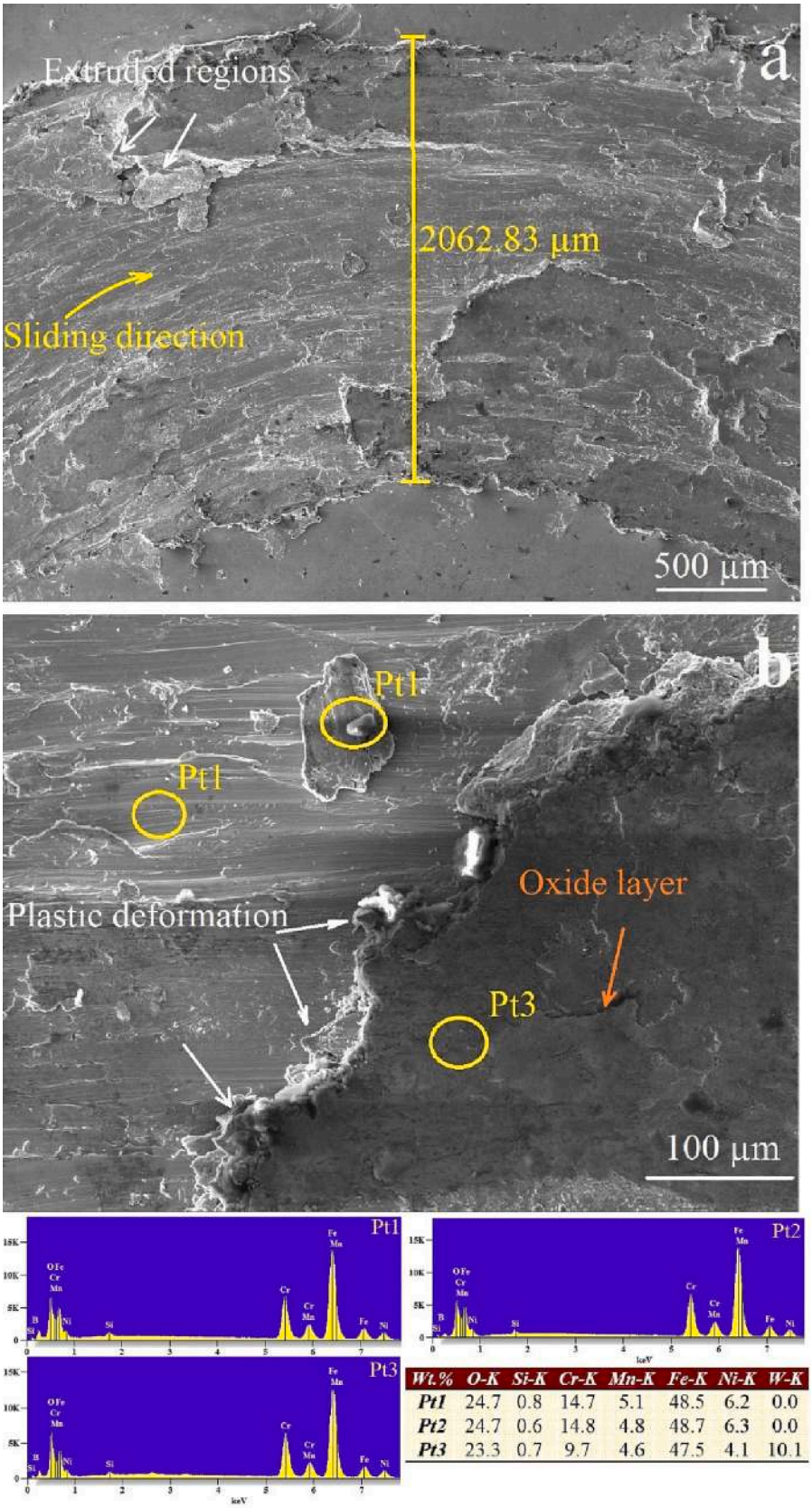

Wt.%	O-K	Si-K	Cr-K	Mn-K	Fe-K	Ni-K	W-K
Pt1	24.7	0.8	14.7	5.1	48.5	6.2	0.0
Pt2	24.7	0.6	14.8	4.8	48.7	6.3	0.0
Pt3	23.3	0.7	9.7	4.6	47.5	4.1	10.1

Fig. 10. SEM surface micrograph and results of EDS point analyses conducted on the worn surface of as-built AISI ER307 stainless steel subjected to wear testing at 500 °C a) 200× b) 1000×.

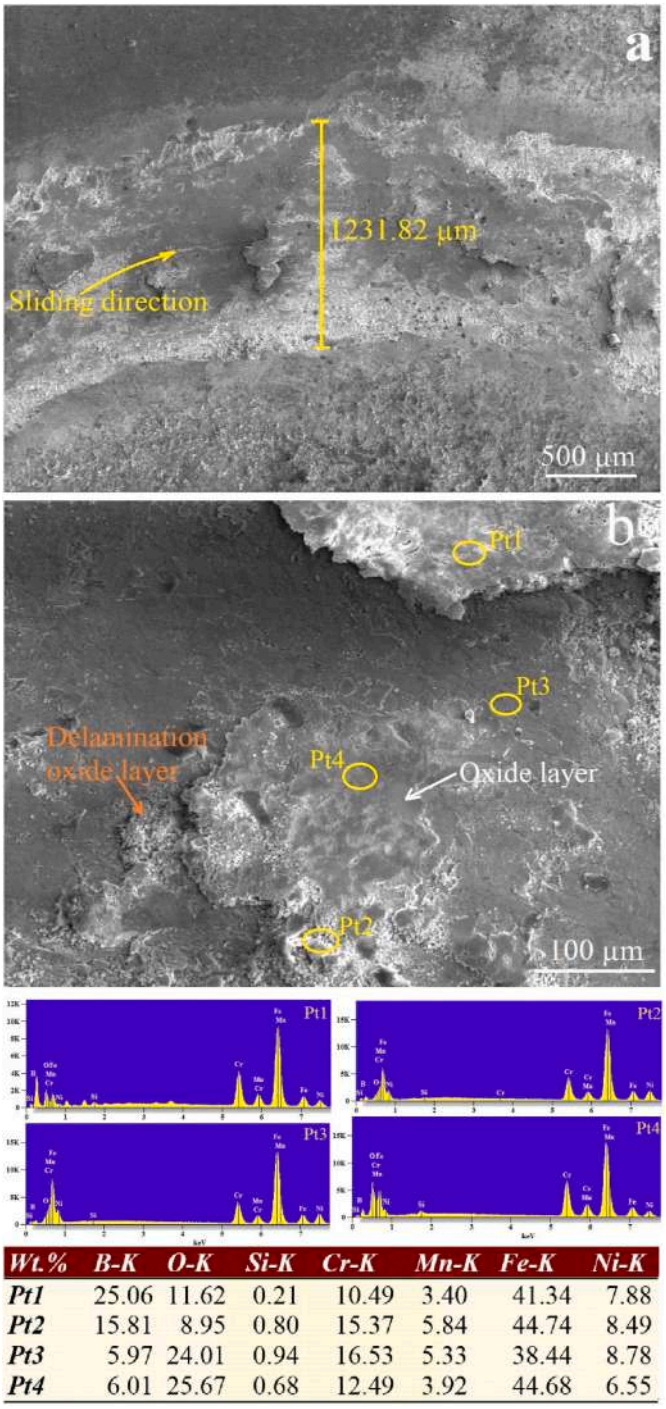

Wt.%	B-K	O-K	Si-K	Cr-K	Mn-K	Fe-K	Ni-K
Pt1	25.06	11.62	0.21	10.49	3.40	41.34	7.88
Pt2	15.81	8.95	0.80	15.37	5.84	44.74	8.49
Pt3	5.97	24.01	0.94	16.53	5.33	38.44	8.78
Pt4	6.01	25.67	0.68	12.49	3.92	44.68	6.55

Fig. 11. SEM surface micrograph and results of EDS point analyses conducted on the worn surface of boronized AISI ER307 stainless steel subjected to wear testing at 500 °C a) 200× b) 1000×.

B and oxygen ratios were determined compared to the samples at room temperature. This indicates that the tribolayer boron oxide layer formed by the effect of high temperature was broken, and the wear took place close to the deeper layer, the Fe_2B layer. As a result, the borided WAAM ER307 stainless steel samples show a remarkable friction reduction and improved wear resistance at room temperature and 500 °C, which indicates excellent self-lubrication performance. Self-lubrication performance may be ascribed to the formation of boron-containing tribofilm on the wear traces, which is generated by the tribochemical reaction between the boride layer and air and self-lubricating properties of the boride layer [33–35].

4. Conclusions

In this work, WAAM fabricated ER307 stainless steel samples were subjected to simultaneous boriding and homogenization heat treatment at 1000 °C for 1 h to enhance the microstructure and to increase their hardness, and wear resistance. Below is a quick summary of the findings and critical outcomes:

1- With the chosen GMAW-based WAAM process parameters, WAAM ER307 stainless steel samples (inner and outer portions) were successfully manufactured without flaws, such as dividing lines, porosity, irregularly shaped oxides, voids, and cracks.
2- Because of the spherical mass transfer mechanism used in WAAM-GMAW procedures, the surface of the stainless steel ER307 produced by WAAM has a rough surface compared to other metal additive manufacturing technics such as powder bed fusion, binder jetting etc. The surface roughness value (R_a) of the as-built sample was about 62.5 µm.
3- The as-built WAAM samples exhibit a microstructure consisting of γ iron-nickel-chromium based solid solution matrix with a face-centered cubic (FCC) crystal structure containing a low amount of delta-ferrites along the austenite grain boundaries (i.e., about 3.5 %) as in wrought austenitic stainless steels.
4- As a result of the boriding procedure, a boride layer of about 30 µm thickness with a 21.45 ± 3.75 GPa hardness and 310 ± 35 GPa elastic modulus was grown on the surface. The surface hardness of as-built samples has increased about four times as a result of this layer. It has been determined that the boride layer formed on the surface is mainly composed of the FeB phase, as well as a low percentage of Fe_2B, Cr_5B_3, and MnB hard borides.
5- The self-lubrication properties of boride layer provided the borided samples to exhibit lower friction coefficient values at both room temperature and 500 °C than the as-built samples. Since wear temperatures have a great effect on the coefficient of friction and volume losses, both the as-built and boronized samples exhibited a higher friction coefficient and were exposed to higher volume losses due to the softening.
6- Temperature has a great influence on the wear behavior of as-built WAAM and borided WAAM ER307 stainless steel samples. As compared to the as-built samples, the borided WAAM ER307 stainless steel samples demonstrated wear resistance that was 31.78 times greater at ambient temperature and 8.04 times greater at 500 °C. The oxidation-assisted delamination that occurs in boride layers at elevated temperature led to a decline in the improvement of wear resistance at elevated temperatures. While the wear mechanism of the as-built samples was abrasive and delamination at room temperature, it turned into oxidation-assisted delamination at 500 °C. On the other hand, the wear mechanism of the borided sample at room temperature was micro-crack and oxidative wear mechanism, and it changed to an oxidation-assisted delamination wear mechanism at 500 °C.

The improvement of the wear resistance provided by the enhancement of the microstructure and mechanical properties of additively manufactured stainless steels by boriding will definitely increase the industrial application of these alloys in the temperature range between room temperature and 500 °C.

CRediT authorship contribution statement

Ali Günen: Conceptualization, Formal analysis, Investigation, Writing – original draft, Writing – review & editing. **Uğur Gürol:** Conceptualization, Methodology, Investigation, Writing – original draft, Writing – review & editing. **Mustafa Koçak:** Validation, Investigation,

Supervision. **Gürel Çam:** Conceptualization, Investigation, Supervision, Writing – original draft.

Declaration of competing interest

The authors declare that they have no known competing financial interests or personal relationships that could have appeared to influence the work reported in this paper.

Data availability

No data was used for the research described in the article.

Acknowledgements

The authors thank Mr. Batuhan Turgut and the R&D Center of the Gedik Welding, Istanbul-Türkiye, for their technical support while manufacturing the WAAM component.

References

[1] D.L. Bourell, Perspectives on additive manufacturing, Annu. Rev. Mater. Res. 46 (2016) 1–18.
[2] H. Chen, L. Ye, Y. Han, C. Chen, J. Fan, Additive manufacturing of W-fe composites using laser metal deposition: microstructure, phase transformation, and mechanical properties, Mater. Sci. Eng. A 811 (2021), 141036.
[3] A. Bandyopadhyay, S. Bose, Additive Manufacturing, 2nd Edition, CRC Press, Boca Raton, FL, USA, 2019.
[4] O. Gokcekaya, T. Ishimoto, S. Hibino, J. Yasutomi, T. Narushima, T. Nakano, Unique crystallographic texture formation in inconel 718 by laser powder bed fusion and its effect on mechanical anisotropy, Acta Mater. 212 (2021), 116876.
[5] L. Wang, J. Xue, Q. Wang, Correlation between arc mode, microstructure, and mechanical properties during wire arc additive manufacturing of 316L stainless steel, Mater. Sci. Eng. A 751 (2019) 183–190.
[6] M. Ziętala, T. Durejko, M. Polański, et al., The microstructure, mechanical properties and corrosion resistance of 316 L stainless steel fabricated using laser engineered net shaping, Mater. Sci. Eng. A 677 (2016) 1–10.
[7] G. Çam, Prospects of producing aluminum parts by wire arc additive manufacturing (WAAM), Mater. Today Proc. 62 (1) (2022) 149–198, https://doi.org/10.1016/j.matpr.2022.02.137.
[8] S. Guler, H.T. Serindag, G. Çam, Wire arc additive manufacturing (WAAM): recent developments and prospects, Eng. Mach. 63 (706) (2022) 82–116, https://doi.org/10.46399/muhendismakina.1085716.
[9] A. Horgar, H. Fostervoll, B. Nyhus, X. Ren, M. Eriksson, O.M. Akselsen, Additive manufacturing using WAAM with AA5183 wire, J. Mater. Process. Technol. 259 (2018) 68–74.
[10] J. Ding, P. Colegrove, F. Martina, S. Williams, R. Wiktorowicz, M.R. Palt, Development of a laminar flow local shielding device for wire+ arc additive manufacture, J. Mater. Process. Technol. 226 (2015) 99–105.
[11] L. Zhu, Y. Luo, J. Han, C. Zhang, J. Xu, D. Chen, Energy characteristics of droplet transfer in wire-arc additive manufacturing based on the analysis of arc signals, Measurement 134 (2019) 804–813.
[12] D. Yang, C. He, G. Zhang, Forming characteristics of thin-wall steel parts by double electrode GMAW based additive manufacturing, J. Mater. Process. Technol. 227 (2016) 153–160.
[13] K.S. Derekar, A review of wire arc additive manufacturing and advances in wire arc additive manufacturing of aluminium, Mater. Sci. Technol. 34 (8) (2018) 895–916.
[14] U. Gurol, S. Dilibal, B. Turgut, M. Kocak, Characterization of a low-alloy steel component produced with wire arc additive manufacturing process using metal-cored wire, Mater. Test. 64 (6) (2022) 755–767.
[15] Y. Ali, P. Henckell, J. Hildebrand, J. Reimann, J.P. Bergmann, S. Barnikol-Oettler, Wire arc additive manufacturing of hot work tool steel with CMT process, J. Mater. Process. Technol. 269 (2019) 109–116.
[16] L. Xue, J. Xiao, Z. Nie, F. Hao, R. Chen, C. Liu, C. Tan, Dynamic response of ti-6.5 Al–1Mo–1V–2Zr-0.1 B alloy fabricated by wire arc additive manufacturing, Mater. Sci. Eng. A 800 (2021), 140310.
[17] M. Xu, Y. Chen, T. Zhang, J. Xie, K. Wei, S. Wang, L. Yin, Effect of post-heat treatment on microstructure and mechanical properties of nickel-based superalloy fabricated by ultrasonic-assisted wire arc additive manufacturing, Mater. Sci. Eng. A 863 (2022), 144548.
[18] A. Gunen, U. Gurol, M. Kocak, G. Çam, Investigation into the influence of boronizing on the wear behavior of additively manufactured Inconel 625 alloy at elevated temperature, Prog. Addit. Manuf. (2023), https://doi.org/10.1007/s40964-023-00398-8.
[19] Q. Shen, X. Kong, X. Chen, Fabrication of bulk Al-co-cr-fe-ni high-entropy alloy using combined cable wire arc additive manufacturing (CCW-AAM): microstructure and mechanical properties, J. Mater. Sci. Technol. 74 (2021) 136–142.
[20] Y. Yang, J. Hu, X.Y. Liu, W. Xu, B. Li, G.P. Ling, Y.Z. Tian, Post treatment of an additively manufactured composite consisting of 304L stainless steel and CoCrFeMnNi high-entropy alloy, Mater. Sci. Eng. A 831 (2022), 142104.
[21] U. Gurol, B. Turgut, N. Gulecyuz, S. Dilibal, M. Kocak, Development of multi-material components via robotic wire arc additive manufacturing, Int. J. 3D Printing Tech. Dig. Ind. 5 (3) (2021) 721–729.
[22] M. Ezer, G. Çam, A study on microstructure and mechanical performance of gas metal arc welded AISI 304L joints, Mater. Sci. Eng. Technol. 53 (9) (2022) 1043–1052.
[23] H.T. Serindag, G. Çam, Microstructure and mechanical properties of gas metal arc welded AISI 430/AISI 304 dissimilar stainless steels butt joints, J. Phys. Conf. Ser. 1777 (2021), 012047.
[24] G. Çam, S. Erim, C. Yeni, M. Kocak, Determination of mechanical and fracture properties of laser beam welded steel joints, Weld. J. 78 (6) (1999) 193s–201s.
[25] W. Jin, C. Zhang, S. Jin, Y. Tian, D. Wellmann, W. Liu, Wire arc additive manufacturing of stainless steels: a review, Appl. Sci. 10 (5) (2020) 1563.
[26] X. Chen, J. Li, X. Cheng, B. He, H. Wang, Z. Huang, Microstructure and mechanical properties of the austenitic stainless steel 316L fabricated by gas metal arc additive manufacturing, Mater. Sci. Eng. A 703 (2017) 567–577.
[27] U.S. Bertoli, G. Guss, S. Wu, M.J. Matthews, J.M. Schoenung, In-situ characterization of laser-powder interaction and cooling rates through high-speed imaging of powder bed fusion additive manufacturing, Mater. Des. 135 (2017) 385–396.
[28] F. Caiazzo, V. Alfieri, Laser-aided directed energy deposition of steel powder over flat surfaces and edges, Materials 11 (3) (2018) 435.
[29] A. Caballero, J. Ding, S. Ganguly, S. Williams, Wire+ arc additive manufacture of 17–4 PH stainless steel: effect of different processing conditions on microstructure, hardness, and tensile strength, J. Mater. Process. Technol. 268 (2019) 54–62.
[30] T.A. Rodrigues, J.D. Escobar, J. Shen, et al., Effect of heat treatments on 316 stainless steel parts fabricated by wire and arc additive manufacturing: microstructure and synchrotron X-ray diffraction analysis, Addit. Manuf. 48 (2021), 102428.
[31] Y. Zhang, F. Cheng, S. Wu, Improvement of pitting corrosion resistance of wire arc additive manufactured duplex stainless steel through post-manufacturing heat-treatment, Mater. Charact. 171 (2021), 110743.
[32] R. Duraisamy, S.M. Kumar, A.R. Kannan, N.S. Shanmugam, K. Sankaranarayanasamy, M.R. Ramesh, Tribological performance of wire arc additive manufactured 347 austenitic stainless steel under unlubricated conditions at elevated temperatures, J. Manuf. Process. 56 (2020) 306–321.
[33] J.N. Panda, B.C. Wong, E. Medvedovski, P. Egberts, Enhancement of tribo-corrosion performance of carbon steel through boronizing and BN-based coatings, Tribol. Int. 153 (2021), 106666.
[34] Y. Zhang, W. Whx, Y. Chen, J. Dong, S. Yin, K. Hua, H. Wang, Characterization of the microstructure and self-lubrication properties of a AlCoCrFeNi2.1 eutectic high-entropy alloy with powder-pack boronizing, Mater. Charact. 191 (2022), 112118.
[35] J. Dong, H. Wu, Y. Chen, Y. Zhang, Y. Wu, S. Yin, H. Wang, Study on self-lubricating properties of AlCoCrFeNi2.1 eutectic high entropy alloy with electrochemical boronizing, Surf. Coat. Technol. 433 (2022), 128082.
[36] M.V. Çakir, A comparative study on tribocorrosion wear behavior of boride and vanadium carbide coatings produced by TRD on AISI D2 steel, Prot. Met. Phys. Chem. Surf. 58 (3) (2022) 562–573.
[37] M.S. Karakaş, A. Günen, C. Çarboğa, Y. Karaca, M. Demir, Y. Altınay, A. Erdoğan, Microstructure, some mechanical properties and tribocorrosion wear behavior of boronized Al0.07Co1.26Cr1.80Fe1.42Mn1.35Ni1.10 high entropy alloy, J. Alloys Compd. 886 (2021), 161222.
[38] E. Atar, E.S. Kayali, H. Cimenoglu, Characteristics and wear performance of borided Ti6Al4V alloy, Surf. Coat. Technol. 202 (19) (2008) 4583–4590.
[39] L.A. Arteaga-Hernandez, C.A. Cuao-Moreu, C.E. Gonzalez-Rivera, M. Alvarez-Vera, J.A. Ortega-Saenz, M.A.L. Hernandez-Rodriguez, Study of boriding surface treatment in the tribological behavior of an AISI 316L stainless steel, Wear 477 (2021), 203825.
[40] I. Campos-Silva, E.J. Hernández-Ramirez, A. Contreras-Hernández, J.L. Rosales-Lopez, E. Valdez-Zayas, I. Mejía-Caballero, J. Martínez-Trinidad, Pulsed-DC powder-pack boriding: growth kinetics of boride layers on an AISI 316 L stainless steel and inconel 718 superalloy, Surf. Coat. Technol. 421 (2021), 127404.
[41] R.A. García-León, J. Martínez-Trinidad, R. Zepeda-Bautista, I. Campos-Silva, A. Guevara-Morales, J. Martínez-Londoño, J. Barbosa-Saldaña, Dry sliding wear test on borided AISI 316L stainless steel under ball-on-flat configuration: a statistical analysis, Tribol. Int. 157 (2021), 106885.
[42] I. Gunes, I. Yıldız, Investigation of adhesion and tribological behavior of borided AISI 310 stainless steel, Matéria (Rio de Janeiro) 21 (2016) 61–71.
[43] A. Gunen, M. Ulutan, M. Gok, B. Kurt, N. Orhan, Friction and wear behaviour of borided AISI 304 stainless steel with nano particle and micro particle size of boriding agents, J. Balkan Tribological Assoc. 20 (3) (2014).
[44] S. Taktak, Tribological behaviour of borided bearing steels at elevated temperatures, Surf. Coat. Technol. 201 (6) (2006) 2230–2239.
[45] U. Gürol, Welding of high manganese austenitic cast steels using stainless steel covered electrode, Int. J. Met. (2022) 1–13.
[46] A. Günen, U. Gürol, M. Koçak, G. Çam, Investigation into the influence of boronizing on the wear behavior of additively manufactured inconel 625 alloy at elevated temperature, Prog. Addit. Manuf. (2023) 1–21.
[47] W.C. Oliver, G.M. Pharr, Nanoindentation in materials research: past, present, and future, MRS Bull. 35 (11) (2010) 897–907, https://doi.org/10.1557/mrs2010.717.

[48] M.S. Rahman, J. Ding, A. Beheshti, X. Zhang, A.A. Polycarpou, Helium tribology of inconel 617 at elevated temperatures up to 950° C: parametric study, Nucl. Sci. Eng. 193 (9) (2019) 998–1012.
[49] M. Kulka, N. Makuch, A. Piasecki, Nanomechanical characterization and fracture toughness of FeB and Fe2B iron borides produced by gas boriding of armco iron, Surf. Coat. Technol. 325 (2017) 515–532.
[50] M.S. Gok, Y. Kucuk, A. Erdogan, M. Oge, E. Kanca, A. Gunen, Dry sliding wear behavior of borided hot-work tool steel at elevated temperatures, Surf. Coat. Technol. 328 (2017) 54–62.
[51] A. Gunen, Properties and high temperature dry sliding wear behavior of boronized inconel 718, Metall. Mater. Trans. A 51 (2) (2020) 927–939.
[52] U. Gurol, Welding of high manganese austenitic cast steels using stainless steel covered electrode, Inter Metalcast (2022), https://doi.org/10.1007/s40962-022-00834-5.
[53] C. Chen, T.T. Feng, G.R. Sun, H.J. Zhang, Microstructure and mechanical characteristics of ER307 stainless steel thin-wall parts in wire arc additive manufacturing hybrid interlayer high-speed friction, Manuf. Lett. 33 (2022) 42–45.
[54] J.W. Fu, Y.S. Yang, J.J. Guo, Formation of a blocky ferrite in fe-cr-ni alloy during directional solidification, J. Cryst. Growth 311 (2009) 3661–3666.
[55] W. Yangfan, C. Xizhang, S. Chuanchu, Microstructure and mechanical properties of inconel 625 fabricated by wire-arc additive manufacturing, Surf. Coat. Technol. 374 (2019) 116–123.
[56] B. Xie, J.X. Xue, X.H. Ren, Wire arc deposition additive manufacturing and experimental study of 316L stainless steel by CMT + P process, Metals 10 (2020) 1419.
[57] V.T. Le, D.S. Mai, T.K. Doan, H. Paris, Wire and arc additive manufacturing of 308L stainless steel components: optimization of processing parameters and material properties, Eng. Sci. Technol. 24 (4) (2021) 1015–1026.
[58] S. Salahi, A.V. Nemani, M. Ghaffari, J. Lunde, A. Nasiri, On microstructure, crystallographic orientation, and corrosion properties of wire arc additive manufactured 420 martensitic stainless steel: effect of the inter-layer temperature, Addit. Manuf. 46 (2021), 102157.
[59] J. Liu, J. Liu, H. Wang, C. Jiang, W. Huang, Research on adding nano-SiC reinforced wire arc additive manufacturing stainless steel, J. Mater. Eng. Perform. (2022) 1–10.
[60] P.P. Nikam, D. Arun, K.D. Ramkumar, N. Sivashanmugam, Microstructure characterization and tensile properties of CMT-based wire plus arc additive manufactured ER2594, Mater. Charact. 169 (2020), 110671.
[61] A. Günen, B. Kurt, N. Orhan, E. Kanca, The investigation of corrosion behavior of borided AISI 304 austenitic stainless steel with nanoboron powder, Prot. Met. Phys. Chem. Surf. 50 (1) (2014) 104–110.
[62] A. Günen, M.S. Karakaş, B. Kurt, A. Calık, Corrosion behavior of borided AISI 304 austenitic stainless steel, Anti-Corros. Methods Mater. 61 (2) (2014) 112–119.
[63] Y. Kayali, A. Büyüksağiş, I. Güneş, Y. Yalçin, Investigation of corrosion behaviors at different solutions of boronized AISI 316L stainless steel, Prot. Met. Phys. Chem. Surf. 49 (3) (2013) 348–358.
[64] M. Çetin, A. Günen, M. Kalkandelen, M.S. Karakaş, Microstructural, wear and corrosion characteristics of boronized AISI 904L superaustenitic stainless steel, Vacuum 187 (2021), 110145.
[65] E. Mertgenc, O.F. Kesici, Y. Kayali, Investigation of wear properties of borided austenitic stainless steel different temperatures and times, Mater. Res. Express 6 (7) (2019), 076420.
[66] H. Cimenoglu, E. Atar, A. Motallebzadeh, High temperature tribological behaviour of borided surfaces based on the phase structure of the boride layer, Wear 309 (1–2) (2014) 152–158.
[67] G. Kartal, S. Timur, V. Sista, O.L. Eryilmaz, A. Erdemir, The growth of single Fe2B phase on low carbon steel via phase homogenization in electrochemical boriding (PHEB), Surf. Coat. Technol. 206 (7) (2011) 2005–2011.
[68] I. Gunes, A.G. Çelik, Surface characterization of borided S220 rebar, J. Charact. 1 (2) (2021) 66–70.
[69] F.E. Mariani, G.C. Rêgo, P.G. Bonella, A.L. Neto, G.E. Totten, L.C. Casteletti, Wear resistance of niobium carbide layers produced on gray cast iron by thermoreactive treatments, J. Mater. Eng. Perform. (2020) 1–7.
[70] A. Günen, B. Soylu, Ö. Karakaş, Titanium carbide coating to improve surface characteristic, wear and corrosion resistance of spheroidal graphite cast irons, Surf. Coat. Technol. 437 (2022), 128280.
[71] X.-Y. Zhao, M. Togaru, Q.-Y. Guo, C.R. Weinberger, L. Lamberson, G.B. Thompson, Carbon influence on fracture toughness of niobium carbides, J. Eur. Ceram. Soc. 39 (2019) 5167–5173.
[72] O. Reyes-Carcaño, J. Martínez-Trinidad, A. Meneses-Amador, G.A. Rodríguez-Castro, I. Campos-Silva, U. Figueroa-López, Scratch test in boride layers: influence of indenter tip radius on failure mechanisms, Mater. Lett. 315 (2022), 131918.
[73] S. Şahin, Effects of boronizing process on the surface roughness and dimensions of AISI 1020, AISI 1040 and AISI 2714, J. Mater. Process. Technol. 209 (4) (2009) 1736–1741.
[74] A.P. Krelling, C.E. Da Costa, J.C.G. Milan, E.A.S. Almeida, Micro-abrasive wear mechanisms of borided AISI 1020 steel, Tribol. Int. 111 (2017) 234–242.
[75] M.A. Doñu-Ruiz, N. López-Perrusquia, A. Renteria-Salcedo, M. Flores-Martinez, E. Rodriguez-De Anda, S. Muhl, E. García, Tribocorrosion behavior of boride coating on CoCrMo alloy produced by thermochemical process in 0.35% NaCl solution, Surf. Coat. Technol. 425 (2021), 127698.
[76] I. Campos-Silva, A.D. Contla-Pacheco, U. Figueroa-López, J. Martínez-Trinidad, A. Garduño-Alva, M. Ortega-Avilés, Sliding wear resistance of nickel boride layers on an inconel 718 superalloy, Surf. Coat. Technol. 378 (2019), 124862.
[77] A. Erdoğan, Investigation of high temperature dry sliding behavior of borided H13 hot work tool steel with nanoboron powder, Surf. Coat. Technol. 357 (2019) 886–895.
[78] C. Li, B. Shen, G. Li, C. Yang, Effect of boronizing temperature and time on microstructure and abrasion wear resistance of Cr12Mn2V2 high chromium cast iron, Surf. Coat. Technol. 202 (24) (2008) 5882–5886.
[79] C.D. Reséndiz-Calderon, G.A. Rodríguez-Castro, A. Meneses-Amador, I.E. Campos-Silva, J. Andraca-Adame, M.E. Palomar-Pardavé, E.A. Gallardo-Hernández, Micro-abrasion wear resistance of borided 316L stainless steel and AISI 1018 steel, J. Mater. Eng. Perform. 26 (11) (2017) 5599–5609.
[80] A. Günen, K.M. Döleker, M.E. Korkmaz, M.S. Gök, A. Erdogan, Characteristics, high temperature wear and oxidation behavior of boride layer grown on nimonic 80A ni-based superalloy, Surf. Coat. Technol. 409 (2021), 126906.
[81] C.X. Li, T. Bell, Sliding wear properties of active screen plasma nitrided 316 austenitic stainless steel, Wear 256 (11–12) (2004) 1144–1152.
[82] Y. Birol, High temperature sliding wear behaviour of inconel 617 and stellite 6 alloys, Wear 269 (2010) 664–671.
[83] C. Thomas, P. Tait, The performance of alloy 625 in long-term intermediate temperature applications, Int. J. Press. Vessel. Pip. 59 (1–3) (1994) 41–49.
[84] M. Bahshwan, C.W. Myant, T. Reddyhoff, M.S. Pham, The role of microstructure on wear mechanisms and anisotropy of additively manufactured 316L stainless steel in dry sliding, Mater. Des. 196 (2020), 109076.
[85] I. Campos-Silva, S. Bernabé-Molina, D. Bravo-Bárcenas, J. Martínez-Trinidad, G. Rodríguez-Castro, A. Meneses-Amador, Improving the adhesion resistance of the boride coatings to AISI 316L steel substrate by diffusion annealing, J. Mater. Eng. Perform. 25 (9) (2016) 3852–3862.
[86] A. Meneses-Amador, D. Blancas-Pérez, R. Corpus-Mejía, G.A. Rodríguez-Castro, J. Martínez-Trinidad, L.F. Jiménez-Tinoco, Adhesive and cohesive strength in FeB/Fe2B systems, J. Mater. Eng. Perform. 27 (5) (2018) 2089–2098.
[87] A. Günen, B. Kurt, İ. Somunkıran, E. Kanca, N. Orhan, The effect of process conditions in heat-assisted boronizing treatment on the tensile and bending strength characteristics of the AISI-304 austenitic stainless steel, Phys. Met. Metallogr. 116 (9) (2015) 896–907.
[88] G. Laird II, W.K. Collins, R. Blickensderfer, Crack propagation and spalling of white cast iron balls subjected to repeated impacts, Wear 124 (2) (1988) 217–235.
[89] Y. Ahn, N.G. Cho, S.H. Lee, D. Lee, Lateral crack in abrasive wear of brittle materials, JSME Int. J. Ser. A Solid Mech. Mater. Eng. 46 (2) (2003) 140–144.
[90] N. Tenwick, S.W.E. Earles, A simplified theory for the oxidative wear of steels, Wear 18 (5) (1971) 381–391.
[91] M. Tripathy, M. Munther, K. Davami, A. Beheshti, Surface property study of additively manufactured inconel 625 at room temperature and 510 °C, Manuf. Lett. 26 (2020) 69–73.
[92] S.Q. Wang, M.X. Wei, F. Wang, Y.T. Zhao, Transition of elevated-temperature wear mechanisms and the oxidative delamination wear in hot-working die steels, Tribol. Int. 43 (3) (2010) 577–584.